applied sciences

MDPI

Article

Integrated Attenuation Compensation and Q-Constrained Inversion for High-Resolution Reservoir Characterization in the Ordos Basin

Yugang Yang [1], Jingtao Zhao [1,2,*], Tongjie Sheng [1], Hongjie Peng [1], Qin Zhang [3,4] and Zhen Qiu [3,4]

[1] College of Geoscience and Survey Engineering, China University of Mining and Technology (Beijing), Beijing 100083, China; bqt2400202035@student.cumtb.edu.cn (Y.Y.); bqt2300202029@student.cumtb.edu.cn (T.S.); bqt2200202002t@student.cumtb.edu.cn (H.P.)
[2] College of Water Sciences, Beijing Normal University, Beijing 100875, China
[3] PetroChina Research Institute of Petroleum Exploration and Development, Beijing 100083, China; zhangqin2169@petrochina.com.cn (Q.Z.); qiuzhen316@163.com (Z.Q.)
[4] National Energy Shale Gas R & D (Experiment) Center, Langfang 065007, China
* Correspondence: diffzjt@163.com

Abstract

Quantitative seismic characterization of transitional shale gas resources in the Da Ning–Ji Xian area, Ordos Basin, is severely hampered by complex coal-measure stratigraphy and rapid lithological variations. These challenges are critically exacerbated by severe signal attenuation from a thick loess overburden and multiple coal seams, which significantly degrades vertical resolution and undermines the reliability of quantitative interpretation. To surmount these obstacles, this study proposes an integrated, attenuation-centric inversion workflow that systematically rectifies attenuation effects as a foundational pre-conditioning step. The novelty of this study lies in establishing a systematic workflow where a data-driven, spatially variant Q-estimation is used as a crucial pre-conditioning step to guide a robust inverse Q-filtering, enabling a high-fidelity quantitative inversion for shale gas parameters in a geological setting with severe attenuation. The proposed workflow begins with a data-driven estimation of a spatially variant quality factor (Q) volume using the Local Centroid Frequency Shift (LCFS) method. This crucial Q-volume then guides a robust post-stack inverse Q-filtering process, engineered to restore high-frequency signal components and correct phase distortions, thereby substantially broadening the effective seismic bandwidth. With the seismic data now compensated for attenuation, high-resolution shale gas parameters, including Total Organic Carbon (TOC), are quantitatively derived through post-stack simultaneous inversion. Application of the workflow to field data yields an inverted volume characterized by improved structural clarity, sharply defined stratigraphic boundaries, and more robust lithological discrimination, highlighting its practical effectiveness. This attenuation-compensated inversion framework thus establishes a robust and transferable methodology for unlocking high-fidelity quantitative interpretation in geological settings previously deemed intractable due to severe seismic attenuation.

Keywords: Q-value inversion; local centroid frequency shift; attenuation compensation; unconventional reservoir characterization; Ordos basin

check for updates

Academic Editor: Nikolaos K. Koukouzas

Received: 26 September 2025
Revised: 23 October 2025
Accepted: 23 October 2025
Published: 28 October 2025

Citation: Yang, Y.; Zhao, J.; Sheng, T.; Peng, H.; Zhang, Q.; Qiu, Z. Integrated Attenuation Compensation and Q-Constrained Inversion for High-Resolution Reservoir Characterization in the Ordos Basin. *Appl. Sci.* **2025**, *15*, 11504. https://doi.org/10.3390/app152111504

Copyright: © 2025 by the authors. Licensee MDPI, Basel, Switzerland. This article is an open access article distributed under the terms and conditions of the Creative Commons Attribution (CC BY) license (https://creativecommons.org/licenses/by/4.0/).

1. Introduction

Seismic attenuation—the inevitable loss of energy as seismic waves propagate through the subsurface—is a fundamental phenomenon with profound implications across the earth

sciences [1–3]. The quality factor Q is a critical parameter linking earthquake seismology, rock physics, and reservoir characterization. Accurate estimation and compensation of attenuation remain essential for high-resolution inversion and reliable quantitative analysis.

A diverse suite of algorithms has been developed to estimate Q, including frequency-domain methods such as the spectral ratio approach and time–frequency techniques like the S-transform [4]. These methods aim to quantify spectral decay precisely, providing both diagnostic information and a foundation for data conditioning. For example, Yin et al. [5] established a compelling link between Q anisotropy and fracture orientation, an insight highly relevant to unconventional reservoir characterization.

Central to this study is inverse Q-filtering, which compensates for amplitude loss and phase dispersion. If uncorrected, these effects severely degrade seismic image fidelity, especially in geologically complex settings [6,7]. In the Ordos Basin, strong coal-seam masking complicates imaging, making conventional seismic attributes ineffective [8–10]. We argue that optimized inverse Q-filtering is a prerequisite for recovering high-resolution signals necessary for reliable inversion of reservoir properties.

The geophysical community has made significant strides in seismic inversion, moving from post-stack acoustic impedance methods [11–13] to sophisticated post-stack simultaneous inversions [14] that can estimate a suite of elastic parameters like P-impedance [15] and S-impedance [16,17] and density [18]. These advanced algorithms, often formulated within a Bayesian [19] or a geostatistical framework, excel at integrating well-log data and geological constraints to produce quantitative models of the subsurface. A critical assumption is that input seismic data accurately represent the Earth's reflectivity. In highly attenuating media, distorted waveforms can lead to non-unique or geologically ambiguous results, where derived properties reflect attenuation artifacts as much as lithology.

Our investigation focuses on the Daji Block, located within the Jinxi Flexural Belt—a second-order tectonic unit on the southeastern margin of the multi-cycle cratonic Ordos Basin [20–22]. During the Late Paleozoic, this area was a dynamic depositional nexus, transitioning from a marine carbonate platform to deltaic–littoral and eventually continental fluvial systems during the Carboniferous–Permian period. This complex paleo-environmental evolution resulted in a highly heterogeneous stratigraphy [23,24]. The Shanxi Formation, particularly its Shan submember, represents a key interval of this transition and is the primary target for shale gas exploration in the region. It is characterized by the complex interbedding of organic-rich shales, tight sandstones, and problematic coal seams [25–28], which, despite significant exploration progress, continue to pose formidable challenges for high-resolution reservoir characterization. The objective of this study is therefore to develop a geophysical workflow capable of resolving these fine-scale lithological variations and accurately predicting shale reservoir properties within this geologically intricate setting.

While previous studies have acknowledged the geological complexities of the Shanxi Formation, conventional quantitative interpretation workflows often fail to adequately address the severe signal degradation preceding the inversion step. This paper presents an integrated seismic inversion framework, predicated on the principle that robust attenuation compensation is not an optional refinement but a prerequisite for reliable reservoir characterization in this setting. Our methodology begins with a data-driven estimation of the interval Q-field, tailored to the specific stratigraphic conditions of the Da Ning–Ji Xian area [29–31]. This Q model then informs a targeted post-stack inverse Q-filtering application designed specifically to counteract the pronounced masking effects of the region's prevalent coal seams [32–34]. The resultant, resolution-enhanced seismic volume serves as the input for a subsequent post-stack simultaneous inversion. We hypothesize that this systematic, physics-based data conditioning will unlock a level of detail in key reservoir property models (e.g., Total Organic Carbon, porosity) that remains inaccessible to standard

approaches, thereby providing a more robust and geologically plausible framework for sweet-spot delineation in these challenging transitional shale systems.

2. Geological Setting

Our study area, the Da Ning–Ji Xian (Daji) Block, is located within the Jinxi Flexural Belt on the eastern margin of the Ordos Basin, a large multi-cycle intracratonic basin in northern China [35–37] (Figure 1). The Late Paleozoic stratigraphy of this region reflects a dynamic paleoenvironmental evolution, transitioning from a stable marine carbonate platform to a complex deltaic–littoral system and ultimately to a continental depositional regime during the Carboniferous–Permian period [35,38,39]. This interval exhibits a highly heterogeneous assemblage of thin, interbedded organic-rich shales, tight sandstones, and thick coal seams, including the prominent No. 5 coal bed near its upper boundary [40–42].

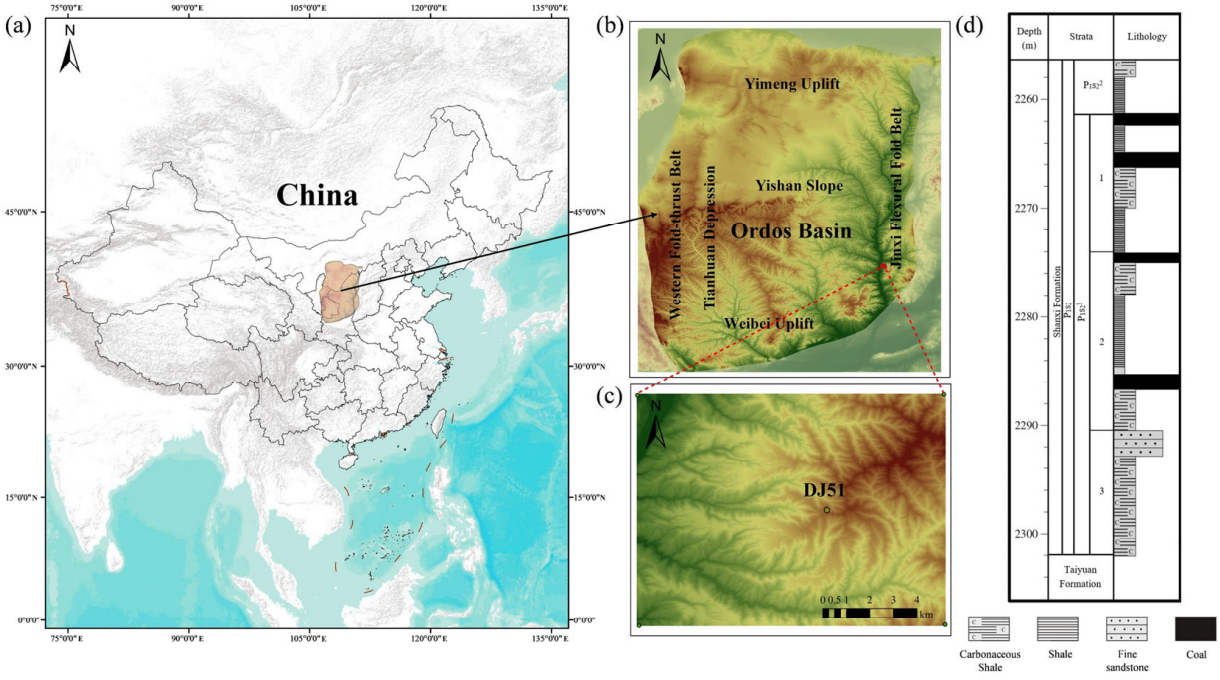


Figure 1. Regional and Local Geological Setting of the Da Ning–Ji Xian Area, Ordos Basin [43]. (**a**) Location of the Ordos Basin in China. (**b**) Regional structure map of the Ordos Basin. (**c**) Tectonic map of the study area. (**d**) Stratigraphic maps of the Shan-2 in the Shanxi Formation in DJ51.

This intricate geological framework presents a formidable challenge for seismic characterization, rendering conventional quantitative methods inadequate. The severe signal degradation originates from the surface downwards; a thick loess overburden and the interspersed coal seams act as highly attenuative layers, reducing the main frequency near the target to approximately 32 Hz and narrowing the effective bandwidth (5–80 Hz) [44,45]. Compounding this issue is a profound scale mismatch between the seismic resolution and the geological target. The theoretical vertical resolution of the raw seismic data is approximately 33 m, an order of magnitude larger than the average sandstone reservoir thickness of only 4.2 m, rendering these reservoirs seismically invisible as discrete units [46,47].

This challenge is further amplified by the non-unique seismic signatures of the varied lithological combinations (shale, sandstone, coal) [48,49], which confound standard inversion and make direct sandstone identification from the raw data nearly impossible. The Daji Block therefore serves not merely as a study area but as a representative testbed where the limitations of conventional seismic analysis are starkly exposed, and the necessity for an advanced, attenuation-aware characterization workflow becomes paramount.

3. Theory and Methodology

Seismic attenuation and geological complexity in the Da Ning–Ji Xian area severely challenge the reliability of conventional inversion workflows [50,51]. Traditional attenuation compensation and inversion procedures are typically implemented as separate, sequential processes, with inverse Q-filtering often regarded as an optional data-conditioning step. Such separation can leave residual amplitude distortion and phase misalignment uncorrected, ultimately compromising inversion accuracy in highly attenuating settings.

To overcome these limitations, this study proposes an integrated three-stage framework (Figure 2) that couples physics-based inverse Q-filtering with post-stack model-based inversion under a unified physical constraint. The core methodological innovation lies in treating attenuation compensation as an essential prerequisite—not a supplementary refinement—thereby ensuring that inversion is performed on a signal whose spectral and phase integrity has been physically restored. Guided by this principle, the workflow proceeds by first estimating the interval Q-field, which directs a stabilized inverse Q-filtering process. The resulting high-resolution, spectrally balanced dataset then serves as the foundation for post-stack simultaneous inversion, enabling quantitative reservoir characterization even in strongly attenuating and geologically complex environments.

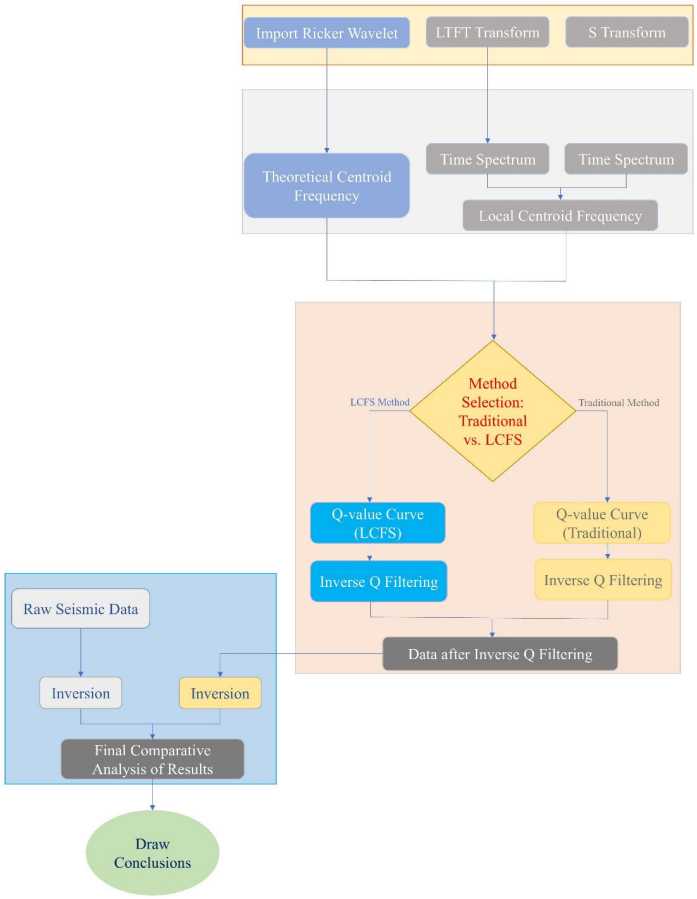


Figure 2. The proposed integrated framework for high-resolution quantitative inversion.

3.1. Q-Factor Estimation via the Local Centroid Frequency Shift (LCFS)

The reliability of the entire workflow depends critically on the accurate estimation of the interval Q-field. This study adopts the centroid frequency shift (CFS) principle originally proposed by Youli Quan and Jerry M. Harris [52], which utilizes the physical relationship between the quality factor (Q) and the progressive downshift of a wavelet's spectral centroid induced by preferential attenuation of high-frequency components.

The centroid frequency f_c and its variance σ_c^2 for a signal with a Fourier amplitude spectrum *F(f)* are defined as its first and second moments, respectively:

$$f_c = \frac{\int_0^\infty fF(f)df}{\int_0^\infty F(f)df} \tag{1}$$

$$\sigma_c^2 = \frac{\int_0^\infty (f - f_c)^2 F(f)df}{\int_0^\infty F(f)df} \tag{2}$$

For non-stationary seismic signals, these definitions are extended into the time–frequency domain to obtain the instantaneous centroid frequency $f_c(t)$ and the instantaneous variance $\sigma_c^2(t)$ using the time–frequency spectrum *B (f, t)*:

$$f_c(t) = \frac{\int_0^\infty fB(f,t)df}{\int_0^\infty B(f,t)df} \tag{3}$$

$$\sigma_c^2(t) = \frac{\int_0^\infty (f - f_c(t))^2 B(f,t)df}{\int_0^\infty B(f,t)df} \tag{4}$$

However, the conventional CFS method suffers from a critical limitation: it assumes that the source wavelet spectrum *S(f)* follows an idealized Gaussian form, which rarely holds for real seismic data:

$$S(f) = S_0 \exp\left[-\frac{(f - f_c(t_0))^2}{2\sigma_c^2(t_0)}\right] \tag{5}$$

t_0 refers to the reference time (or starting time), taken at a shallow reflector or horizon on the seismic record that is assumed to be minimally affected by attenuation. At this reference time, *S(f)* represents the theoretical source wavelet spectrum before significant attenuation, providing the baseline for subsequent Q-estimation calculations.

This unrealistic assumption introduces systematic bias into the estimation of Q. To address this issue, the present study employs the Local Centroid Frequency Shift (LCFS) method, which incorporates shaping regularization [53] to derive a stable local measure of centroid frequency without assuming any global spectral shape.

Following [54], the instantaneous centroid frequency in Equation (3) can be expressed in linear algebraic form as:

$$\mathrm{W} \approx \mathrm{D}^{-1}\mathrm{z} \tag{6}$$

where W denotes the vector of instantaneous centroid frequencies, and D and z are operators derived from the denominator and numerator of Equation (3), respectively. To stabilize this ill-posed problem, a shaping regularization constraint is imposed to ensure a smoothly varying solution. The shaping operator S is defined as:

$$\mathrm{S} = \mathrm{I} - \lambda^2 \mathrm{L} \tag{7}$$

where L represents a finite-difference Laplacian operator and λ is a scaling parameter that controls smoothness. To estimate the local Q factor, we first compute the local centroid frequency f_{loc} using a least-squares formulation:

$$\mathrm{f_{loc}} = \left(\mathrm{D}^T\mathrm{D} + \mathrm{S}^T\mathrm{S}\right)^{-1}\mathrm{D}^T\mathrm{z} \tag{8}$$

where D represents the finite-difference operator applied to the seismic signa z, S is a smoothing operator, and the superscript T denotes the transpose. The scaling parameter embedded in S controls the smoothness of the solution.

A similar derivation is used to obtain the corresponding local variance σ_{loc}^2.

By substituting these locally derived attributes into the Q-estimation equation, we obtain the LCFS formulation for a time-varying Q-field:

$$Q(t) = \frac{\pi(t - t_0)(f_{loc}^2(t) + \sigma_{loc}^2(t))}{f_{loc}(t_0) - f_{loc}(t)} \tag{9}$$

The LCFS approach provides a continuous and stable estimation of the Q-field, remaining robust against noise and data gaps. This stability makes it particularly suitable for the complex geological and seismic conditions encountered in our study area.

3.2. Attenuation Compensation via Stable Inverse Q-Filtering

With a robust, spatially varying Q-field now established, the next step involves analytically compensating for the attenuation effects of amplitude decay and phase dispersion. To achieve this, a stable inverse Q-filtering algorithm is employed, constrained by the previously derived time-varying Q model.

The propagation of a plane wave in a one-dimensional viscoelastic medium is expressed in the frequency domain as:

$$P(\tau, \omega) = P(0, \omega) \exp[-i\omega\tau + \int_0^\tau \frac{i\omega}{2Q(\tau')} d\tau'] \tag{10}$$

where $P(\tau, \omega)$ is the complex wavefield at travel time τ and angular frequency ω, $P(0, \omega)$ is the initial wavefield at $\tau = 0$, and i is the imaginary unit.

The forward Q-filtering operator, which simulates the Earth's intrinsic attenuation effects, is defined as:

$$A(\tau, \omega) = \exp\left[-\int_0^\tau \frac{\omega}{2Q(\tau')} d\tau'\right] \exp\left[i\int_0^\tau \frac{\omega}{2Q(\tau')} \mathrm{sgn}(\omega) d\tau'\right] \tag{11}$$

This operator incorporates two distinct physical processes: a frequency-dependent amplitude decay and a causal phase rotation (dispersion), both governed by the signum function sgn(ω).

Inverse Q-filtering is designed to be the inverse operation, $A^{-1}(\tau, \omega)$ intended to analytically remove this operator from the seismic data [55,56]. However, a major challenge arises because the amplitude compensation term is an exponential gain function that inherently amplifies high-frequency noise, often leading to numerical instability. To mitigate this instability, the stabilized implementation proposed by Yanghua Wang [57] is adopted:

$$P(0, \omega) = P(\tau, \omega) \cdot \left(\frac{\exp\left[\int_0^\tau \frac{\omega}{2Q(\tau')} d\tau'\right]}{1 + \sigma\left(\exp\left[\int_0^\tau \frac{\omega}{Q(\tau')} d\tau'\right] - 1\right)} \right) \cdot \exp\left[-i\int_0^\tau \frac{\omega}{2Q(\tau')} \mathrm{sgn}(\omega) d\tau'\right] \tag{12}$$

where σ represents a small stabilization factor that controls the extent of high-frequency amplification, it is determined through a data-constrained optimization procedure. Specifically, σ is calibrated to achieve an optimal balance between bandwidth recovery and noise suppression, guided by the agreement between the seismic data and well control points, while avoiding non-physical ringing or instability. This data-driven approach ensures that the inverse Q-filtering process is both robust and reliable, without relying on arbitrary

parameter selection. The output of this stage is a seismic dataset with restored bandwidth and phase continuity, providing a high-fidelity input for subsequent quantitative inversion.

3.3. Post-Stack Model-Based Acoustic Impedance Inversion for Reservoir Properties

After restoring the signal's bandwidth and phase integrity, the conditioned post-stack seismic dataset becomes suitable for extracting quantitative reservoir parameters. The adopted approach is a model-based post-stack inversion designed to transform seismic reflection data into a quantitative volume of P-wave acoustic impedance.

The underlying principle assumes that the post-stack seismic trace approximates the zero-offset, or normal-incidence, reflection response of the subsurface [58–60]. Under normal incidence, the reflectivity at an interface is primarily governed by the contrast in P-wave acoustic impedance ($Z_p = V_p \cdot \rho$):

$$R = \frac{Z_{p2} - Z_{p1}}{Z_{p2} + Z_{p1}} \approx \frac{1}{2}\Delta \ln(Z_p) \tag{13}$$

where Z_{p1} and Z_{p2} denote the P-wave impedances of the upper and lower layers, respectively.

The recorded seismic trace S(t) is modeled as the convolution of the normal-incidence reflectivity series R(t) and a source wavelet W(t):

$$\mathrm{S(t)} = \mathrm{W(t)} * \mathrm{R(t)} + \mathrm{N(t)} \tag{14}$$

where N(t) represents the additive noise component.

In this study, a Ricker wavelet with a central frequency is employed as the source wavelet W(t). The Ricker wavelet is widely used in seismic modeling due to its simple, well-defined amplitude spectrum and symmetric shape, which facilitates the analysis of attenuation effects and inversion validation. While broadband constant-amplitude wavelets could provide a more realistic representation of field seismic data, the Ricker wavelet is sufficient for the present study's focus on method demonstration and Q-estimation.

Model-based inversion addresses this inverse problem by iteratively estimating the P-impedance model that best reproduces the observed seismic response. The process begins with constructing a low-frequency model (LFM) from well-log data, which supplies the background impedance trend missing from the band-limited seismic data [61–63]. The inversion algorithm then iteratively perturbs this model until the synthetic seismogram, generated from the updated impedance model, achieves the optimal match with the observed seismic traces [64,65]. This process produces a high-resolution quantitative volume of P-wave impedance, which serves as the foundation for subsequent lithological interpretation and for estimating shale gas evaluation parameters, such as TOC, using established rock-physics relationships.

Furthermore, future work could explore the use of broadband constant-amplitude or field-recorded wavelets to further assess the frequency-dependent behavior of the workflow in more realistic seismic scenarios. This would complement the current study while maintaining the methodological clarity and focus on inverse Q-filtering and quantitative inversion.

4. Results and Discussion

The effectiveness of the proposed attenuation-compensated inversion framework was validated through a multi-stage investigation designed to establish a comprehensive demonstration of its performance advantages. The analysis begins with a demonstration of the theoretical soundness of the LCFS methodology using a synthetic dataset designed to replicate the geological conditions of the study area. The validated workflow was

subsequently applied to a 2D field seismic line from the Da Ning–Ji Xian area to evaluate its performance in Q-field estimation and signal restoration. The investigation culminated in a comparative inversion analysis aimed at quantifying the measurable improvements in reservoir characterization that conventional approaches fail to achieve.

4.1. Synthetic Data Validation

To assess the practical applicability of the LCFS method, it was first tested using a challenging synthetic dataset—a 2D seismic model constructed to replicate the geological characteristics of the study area (Figure 3a). This synthetic model, featuring a constant background Q and multiple reflectors at key intervals (0.1 s, 0.3 s, 0.4 s, and 0.6 s), served as a controlled environment for evaluating the method's fundamental capabilities, with the topmost layer treated as non-attenuative.

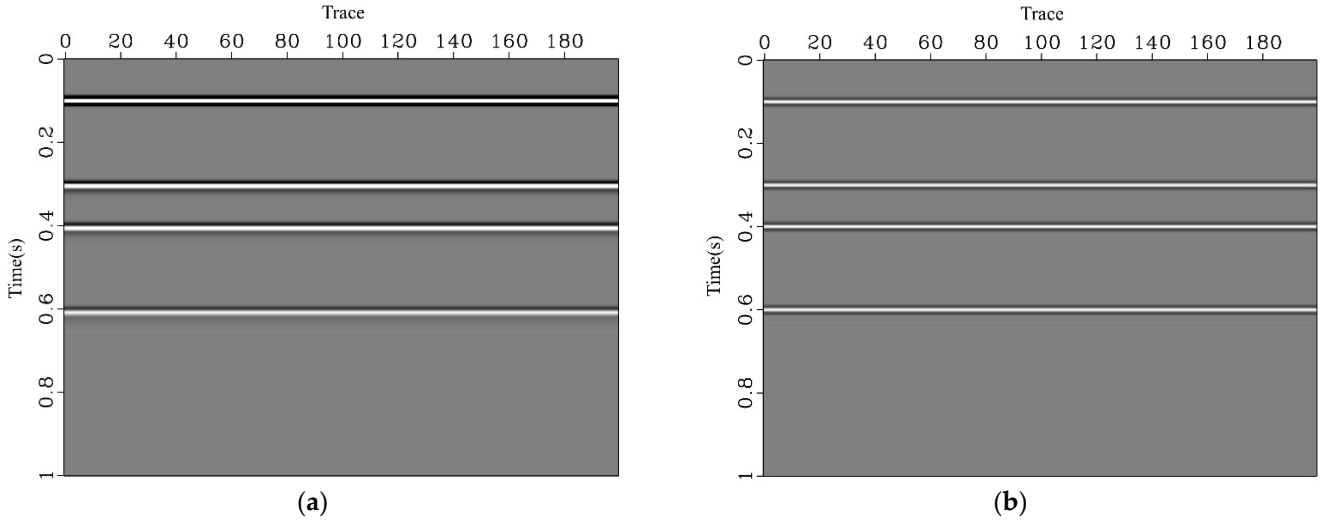


Figure 3. The 2D synthetic model used for methodology validation. (**a**) The layered interval Q-model, featuring a constant background Q-value below the unattenuated first layer. (**b**) The corresponding zero-offset synthetic seismic section generated from the model, exhibiting progressive amplitude decay and waveform broadening with increasing travel time.

A key aspect of attenuation estimation involves determining how to decompose a seismic signal into its time–frequency components [66,67]. The selection of the transform is not merely a technical detail but a foundational decision that dictates the fidelity of all subsequent analysis. The proposed Local Time–Frequency Transform (LTFT)—an adaptive time–frequency transform proposed by Liu and Fomel [68] that utilizes shaping regularization to solve the underdetermined least-squares problem of the adaptive Fourier series—was compared with the widely used S-transform [4,69,70] to evaluate their ability to accurately capture the evolving spectral characteristics of the seismic signal. The LTFT is designed to adjust the frequency range and sampling interval while providing variable resolution in the time direction. The results, illustrated in Figure 4, clearly demonstrate the differences between the two approaches. The S-transform (Figure 4b), though operationally effective, produces a spectrum in which the reflection energy appears smeared and poorly resolved. In contrast, the LTFT (Figure 4a) delivers a sharp, highly resolved spectral representation, where individual seismic events are crisply delineated in both time and frequency.

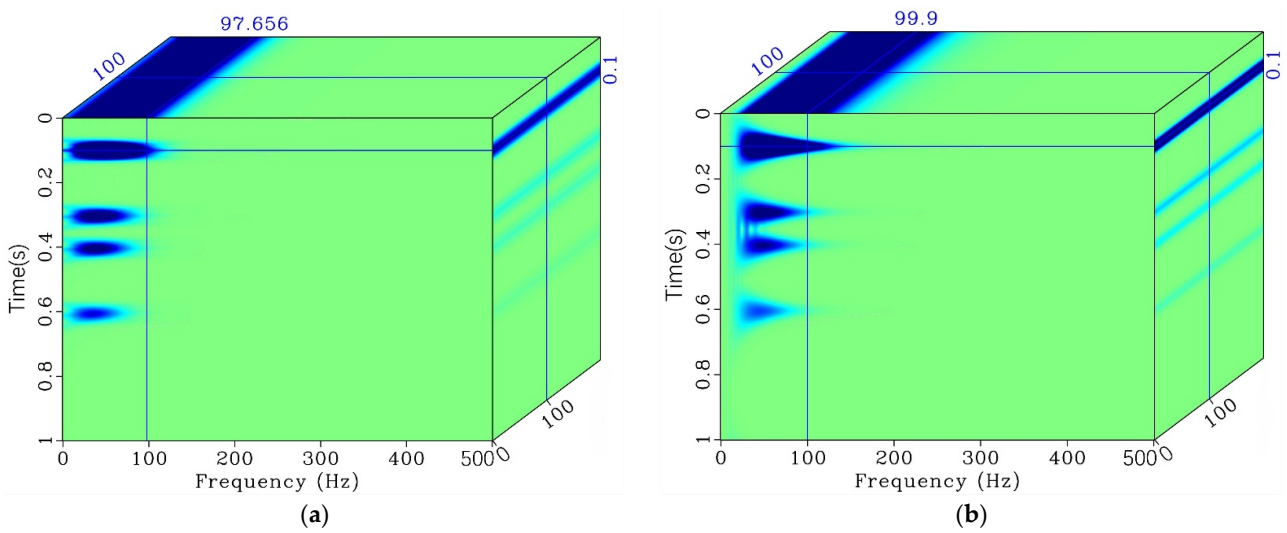


Figure 4. Comparison of time–frequency spectra for a synthetic seismic trace, derived from (**a**) the Local Time–Frequency Transform (LTFT) and (**b**) the S-transform. The color represents the spectral amplitude, with dark blue indicating higher values and green indicating lower values, to highlight the comparative effect.

This enhanced resolving capability proved to be the decisive factor. An accurate local centroid frequency—the cornerstone of the LCFS method—can only be derived from a spectrum that faithfully represents the true signal characteristics. The quantitative implications of this difference are illustrated in Figure 5. The centroid frequency estimated from the LTFT-derived high-fidelity spectrum (blue line) closely follows the theoretical reference (gray line), accurately reproducing the smooth downward trend associated with attenuation. In contrast, the estimate obtained using the S-transform (red line), limited by its smeared spectral representation, exhibits substantial inaccuracies. It shows a consistent systematic overestimation across the entire time window and introduces non-physical high-frequency artifacts, most evident in the irregular breaks along the curve. This experiment clearly established the LTFT as the most reliable foundation for the proposed workflow.

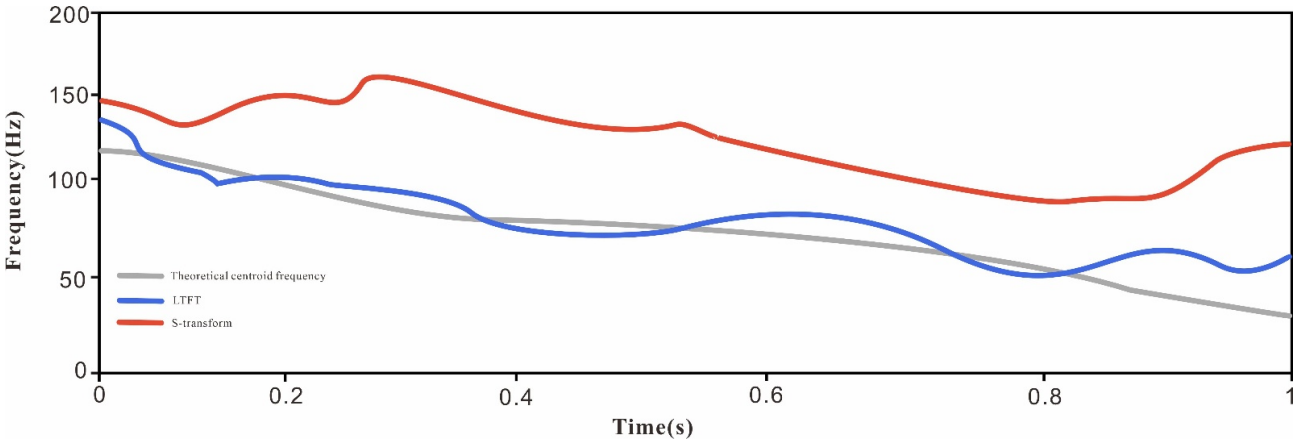


Figure 5. Comparison of the theoretical centroid frequency (gray line) with results from the LCFS method (blue line) and the S-transform method (red line). The LCFS result shows excellent agreement with the theoretical value, while the S-transform result is systematically overestimated.

The substantial difference between the S-transform and LTFT arises from their fundamental approaches to time–frequency localization. The S-transform employs a fixed window for all frequencies, which can smear rapid temporal variations in high-frequency

components, leading to inaccurate spectral representations. In contrast, the Local Time–Frequency Transform (LTFT) is adaptive, providing variable local resolution along the time axis and incorporating shaping regularization to stabilize the least-squares solution. This enables LTFT to extract a high-fidelity spectrum that accurately reflects the evolving characteristics of the seismic signal. Consequently, the local centroid frequency—the cornerstone of the LCFS method—can be precisely estimated. As shown in Figure 5, the centroid frequency derived from the LTFT spectrum (blue line) closely follows the theoretical reference (gray line), accurately reproducing the smooth downward trend due to attenuation. By contrast, the S-transform (red line) exhibits systematic overestimation and introduces non-physical high-frequency artifacts due to its smeared spectral representation. This comparison demonstrates that the enhanced resolving capability of LTFT is the decisive factor, establishing it as the most reliable foundation for the proposed workflow.

With this fundamental challenge addressed, the complete LCFS algorithm was implemented. The estimated Q-field was subsequently used to perform inverse-Q-filtering, effectively compensating for attenuation effects. The compensated section (Figure 3b) clearly demonstrates the effectiveness of the proposed method. The previously distorted signal shows substantial improvement: amplitudes are consistently recovered, phase continuity is restored, and the seismic image exhibits enhanced resolution that reveals fine structural details. This synthetic validation not only confirms the theoretical soundness of the LCFS approach but also demonstrates that, with an appropriate methodological design—particularly in the time–frequency domain—the framework can effectively mitigate attenuation effects and restore the physical integrity of seismic data.

4.2. Field Data Application: Q-Estimation and Attenuation Compensation

Following the successful synthetic validation, the proposed LCFS-based attenuation-compensated inversion workflow was applied to real seismic data from the Da Ning–Ji Xian (Daji) Block within the Ordos Basin. This step aimed to verify the method's robustness under realistic geological and noise conditions, as well as to assess its practical value for reservoir characterization.

To ensure a reliable Q-estimation, which is highly sensitive to amplitude variations, the seismic data was first conditioned with Automatic Gain Control (AGC), as shown in Figure 6b. This essential preprocessing step normalized the energy distribution across the section, preventing the spectral decay of deeper, weaker reflections from being obscured by dominant shallow events. This gain-balanced volume subsequently served as input for time-varying Q-factor estimation using the LCFS method.

The resulting Q-profile (Figure 6c) is not merely a processing output but also serves as an effective diagnostic attribute. It clearly captures the expected background trend of decreasing Q with depth, reflecting cumulative attenuation. More importantly, it reveals a distinct, structurally conformable low-Q anomaly ($Q \approx 60$–80) spatially coincident with the high-amplitude, multi-cycle reflection package near 1.5 s. This data-driven correlation indicates that the target zone represents a region of high intrinsic attenuation, possibly related to geological features such as gas-bearing sands, coal seams, or poorly consolidated shales [71].

Using this detailed Q-field, inverse Q-filtering was applied to compensate for the identified attenuation effects. The transformative impact is demonstrated in the final section (Figure 6d). A visual comparison against the original data (Figure 6a) confirms that the process has achieved more than a superficial enhancement. Phase correction sharpens the seismic wavelets, substantially improving vertical resolution and enabling the delineation of previously obscured stratigraphic features. In addition, amplitude compensation restores the energy of deeper reflectors, enhancing their continuity and structural definition.

Overall, the workflow produces a seismic image that more faithfully represents subsurface reflectivity, providing a reliable basis for subsequent geological interpretation.

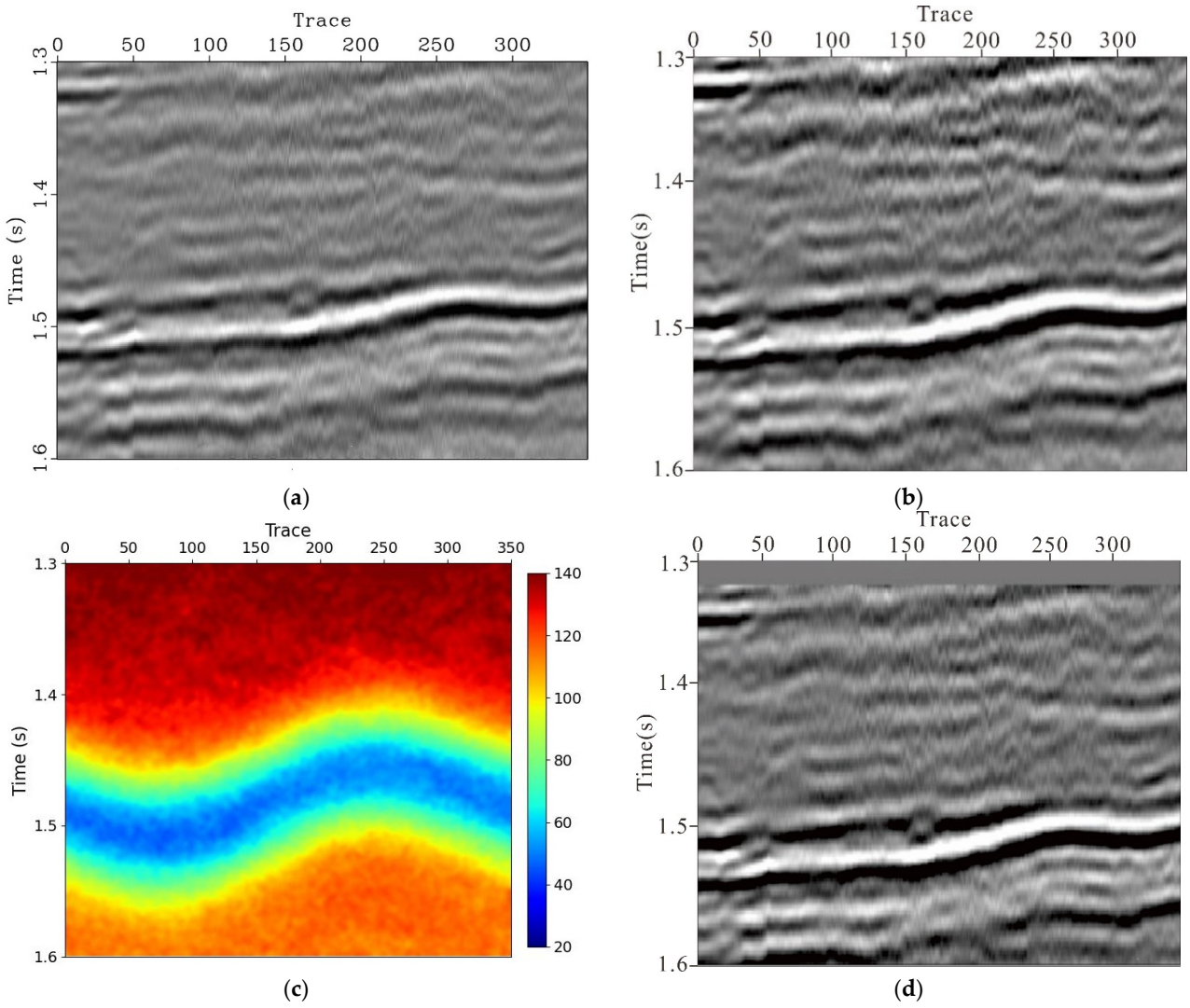


Figure 6. Workflow and results of inverse Q-filtering on a seismic profile from the Ordos Basin. (**a**) Original post-stack seismic section. (**b**) Seismic section after applying Automatic Gain Control (AGC). (**c**) Estimated equivalent time-varying Q-factor profile. (**d**) Seismic section after inverse Q-filtering for attenuation compensation. (Note: The apparent downward time-shift of events in this panel (relative to (**b**)) is primarily due to the different display top boundaries used for visualization, where this panel is intentionally cropped starting from t = 1.3 s; the absolute event timing in the target zone is consistent across all sections).

4.3. Quantitative Inversion and Reservoir Characterization

While enhanced seismic imaging is a valuable outcome, the true scientific and commercial validation of our attenuation compensation framework lies in a more demanding test: its ability to improve the quantitative prediction of reservoir properties. To quantitatively evaluate the impact of this compensation, we moved beyond visual comparison and subjected both the original and our compensated datasets to a full post-stack simultaneous inversion. This parallel analysis serves as a controlled experiment, designed to isolate and quantify how restoring the attenuated components of the seismic signal directly translates into a more reliable characterization of the subsurface.

4.3.1. Building a Constrained Inversion Framework

The post-stack inversion methodology, founded on the convolutional model, necessitated the construction of a robust, low-frequency background velocity model. This model, precisely constrained by available well logs and comprehensive geological interpretation, functioned as the essential framework for the subsequent inversion algorithm [72,73]. Crucially, the entire workflow was conceptualized and executed as an integrated, non-sequential process. This approach was vital for ensuring that the initial model, all inversion parameters, and the final derived acoustic impedance volume were geologically plausible and mutually consistent with the seismic data.

Well–seismic calibration represents a critical foundation of the inversion workflow, establishing a consistent link between well-log measurements and seismic data [74]. Synthetic seismograms were constructed from the P-wave velocity and density logs using the convolutional model and then matched against field seismic traces to derive an accurate time–depth relationship. This process ensures that geological features observed in the logs correspond precisely to their seismic reflections.

As illustrated in Figure 7, the blue trace on the left represents the synthetic seismogram generated from well-log data using a theoretical source wavelet, whereas the red trace denotes the field seismic trace extracted at the well location. The strong phase and amplitude correspondence within the Shan-23 Formation (indicated in the figure) confirms the fidelity and phase stability of the attenuation-compensated data. Minor mismatches outside the target interval arise from natural stratigraphic heterogeneity and the difference in effective bandwidth between logs and seismic data, which are not critical for inversion reliability.

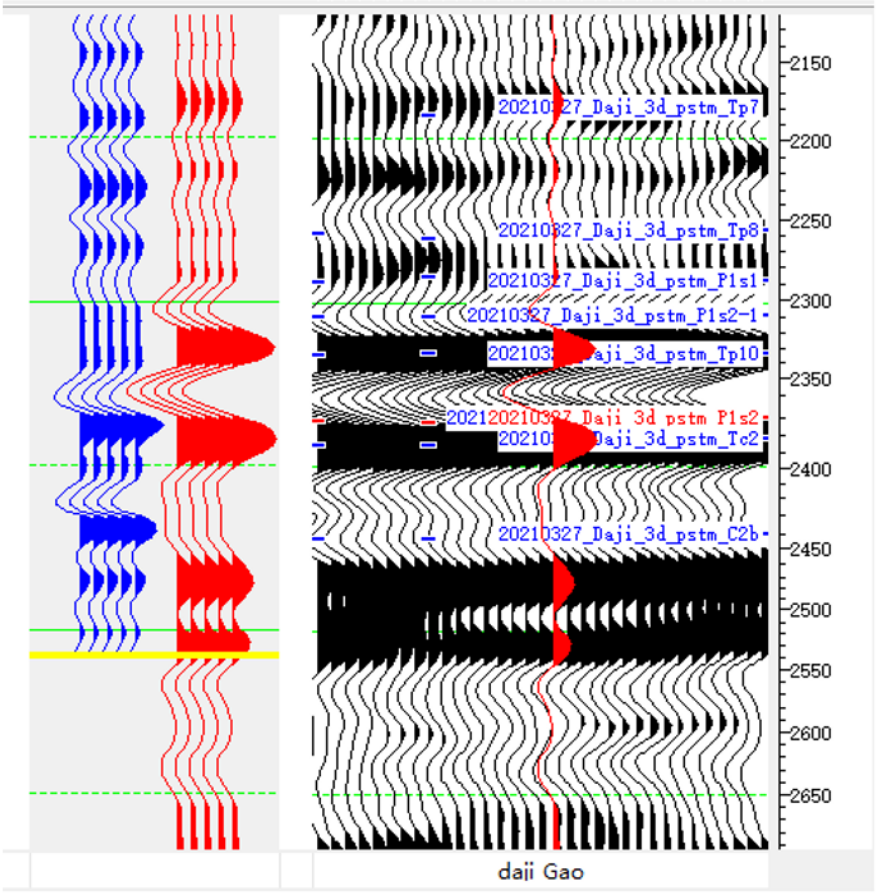


Figure 7. Well–seismic calibration at a key well location.

The panel on the right displays the surrounding seismic section, illustrating how the calibrated trace ties into the broader structural context. For clarity, the figure emphasizes the relative alignment of reflection events rather than absolute recording time; thus, the time axis was omitted intentionally to maintain focus on waveform correspondence within the target zone. The excellent match in the Shan-23 interval provides a high-confidence validation of the compensation and ensures the robustness of the subsequent inversion results.

Following the secure anchoring of the seismic data to geological depth, the focus shifted to the definition of an accurate and representative seismic wavelet. This wavelet is not merely a processing parameter; it constitutes the fundamental seismic "language" used by the inversion to translate reflectivity into reservoir rock properties [75]. An inaccurate wavelet would introduce systemic bias, thereby undermining the integrity of the entire quantitative interpretation. Consequently, we derived a statistical wavelet directly from the most reliable portion of the attenuation-compensated data, utilizing a time window precisely encompassing the target reservoir.

The character of this extracted wavelet, presented in Figure 8, proved to be ideal for high-resolution inversion. Its symmetric, zero-phase form in the time domain ensures that geological boundaries are imaged at their true vertical positions, free from phase-induced artifacts [76]. The corresponding amplitude spectrum (Figure 9) is equally important, revealing a broad and robust bandwidth that is essential for delineating the fine stratigraphy of the target formation.



Figure 8. Characteristics of the statistical wavelet extracted for inversion.

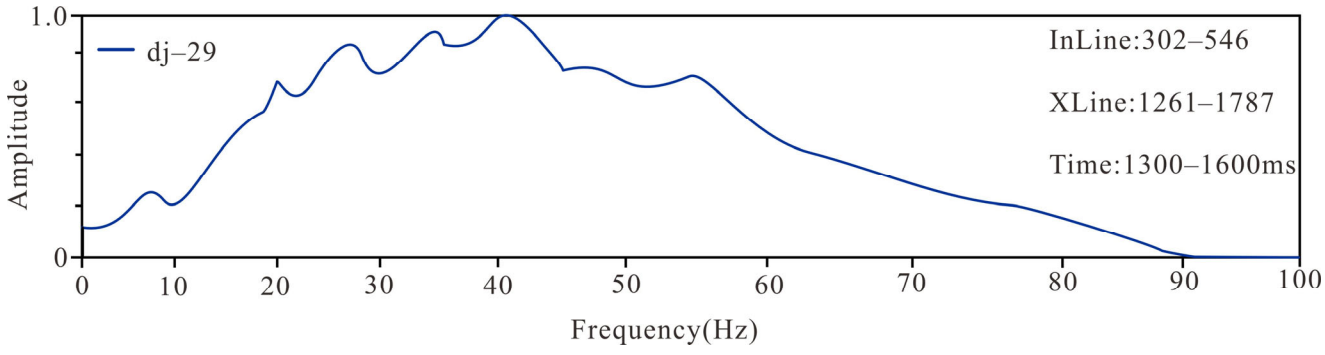


Figure 9. Amplitude spectrum of the seismic data in the target window.

However, a wavelet extracted from a limited window must be objectively validated to confirm it is representative of the broader seismic response. We confirmed this by comparing its spectral signature against the average spectrum of the entire target volume (Figure 9). The remarkable consistency between the two—with both spectra dominated by a potent 15–35 Hz frequency band—provides compelling, data-driven evidence that the derived wavelet is not a local anomaly but a faithful representation of the signal illuminating the Shan-23 member. This validation ensures that the subsequent inversion is built upon a robust and representative geophysical foundation, enabling the resolution of fine-scale geological detail.

To complete the inversion framework and ensure a geologically coherent representation of the subsurface, a low-frequency model was constructed to populate the seismic null band below 10 Hz. This initial model is not an arbitrary background trend; rather, it serves as a critical, geologically driven foundation that robustly guides the inversion towards a plausible solution, particularly in areas of poor seismic data quality.

The construction process involved kriging the P-wave velocity, S-wave velocity, and density logs along a framework of key interpreted horizons. This ensured that the resulting long-wavelength trends accurately reflect the established stratigraphy. Here, kriging denotes a geostatistical interpolation technique that predicts property values at unsampled locations by exploiting the spatial correlation structure among existing data. The method uses a variogram model to assign statistically optimal weights to nearby samples, thereby minimizing estimation variance. In this study, kriging was employed to interpolate the well-log–derived velocity fields across the interpreted horizons, ensuring that the resulting volumes are both geologically consistent and statistically robust. Figure 10 presents a cross-section through the resulting P-velocity volume, which functions as the foundational low-frequency component for the P-impedance inversion. The model distinctly captures the expected large-scale velocity layering: lower velocities in the shallower section (indicated by blue and green hues) gradually transition to higher velocities at depth. A prominent high-velocity layer (deep red) is evident below 1500 ms, which is highly consistent with regional geological knowledge.

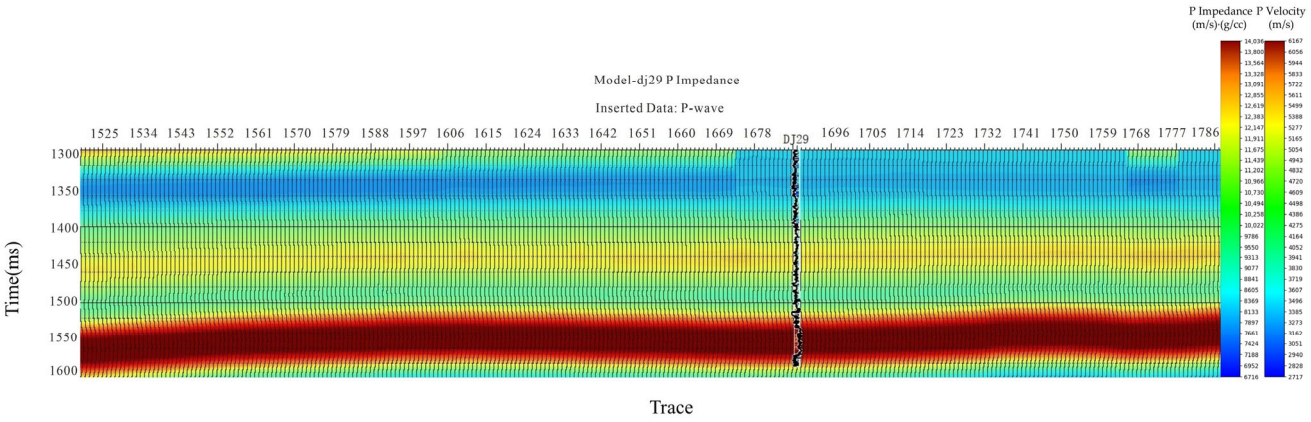


Figure 10. Low-frequency P-impedance model used as an initial constraint for inversion.

The integrity of this low-frequency model is ultimately anchored by its precise tie to the ground-truth well data. As demonstrated in Figure 10, the overlaid P-wave log from well DJ29 exhibits an excellent match with the interpolated background model. This confirms that our methodology accurately captures both the vertical velocity trends and the absolute velocity values at the well location. Consequently, this robust, well-calibrated foundation is essential for ensuring the stability and accuracy of the final impedance inversion result. The synergy of this integrated framework is further validated in the subsequent critical quality

control step, where the well logs, this low-frequency model, and the final high-resolution inversion result all show excellent agreement, thereby confirming the internal consistency of the entire workflow.

The internal consistency of our multi-component model is best visualized at the well location, enabling direct comparison between the foundational elements and the final output. Figure 11 provides this critical quality control check, distinctly displaying the synergy between the three key curves that define the result.

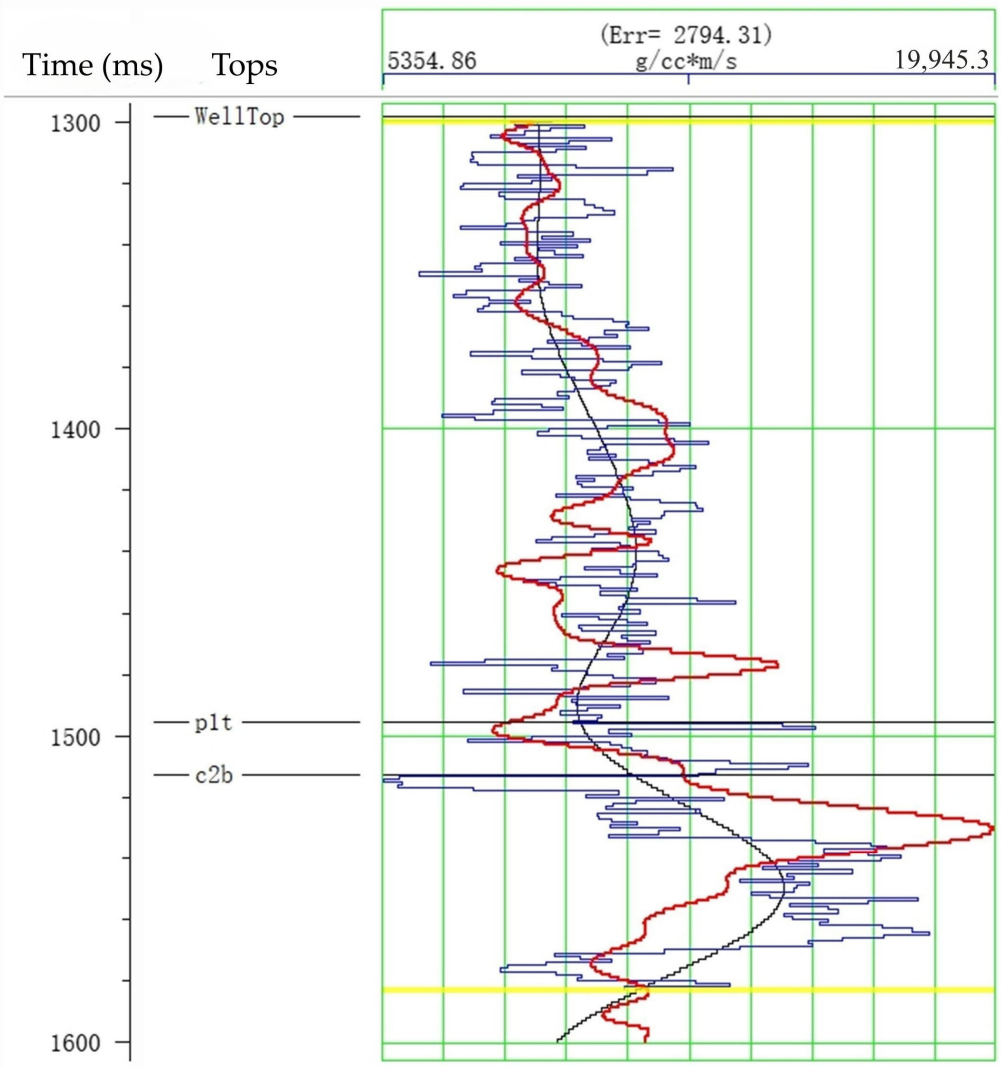


Figure 11. Inversion quality control at the well location: the inverted P-impedance (red) with the initial low-frequency model (black) and the ground-truth P-impedance log (blue). Key formation tops are marked.

The smooth black curve represents the low-frequency model, which establishes the essential long-wavelength trend. Conversely, the jagged blue curve is the original, high-frequency P-impedance well log, representing the ground-truth data we aim to honor. The red curve illustrates the final, high-resolution inversion result, which effectively integrates the low-frequency model with the high-frequency information derived from the seismic data.

Within the primary zone of interest (approximately 1300–1600 ms), the alignment among all three curves is excellent. The red inversion result successfully captures the major peaks and troughs of the blue well log, thereby demonstrating the accurate reintroduction of high-frequency detail by the seismic data. Importantly, both the well log and the inversion

result correctly follow the broader trend established by the black low-frequency model. This close three-way correspondence provides strong support for the fidelity of our inversion framework within the target zone. Below this interval, the match predictably deteriorates, attributable to a combination of decreasing seismic signal quality and potential artifacts in the deeper portions of the well log. This critical observation allows us to confidently focus subsequent geological interpretation on the well-calibrated upper section, where the model's reliability is highest.

4.3.2. Impact on P-Impedance: The Foundation for Quantitative Interpretation

Having confirmed the fidelity of the inversion framework, it was then applied to the attenuation-compensated dataset to derive the final P-impedance volume. Figure 12 presents a key cross-section from this volume, intersecting the ground-truth calibration point, well DJ29. The resulting P-impedance section provides a high-fidelity image of the subsurface elastic properties, forming the essential foundation for subsequent quantitative interpretation.

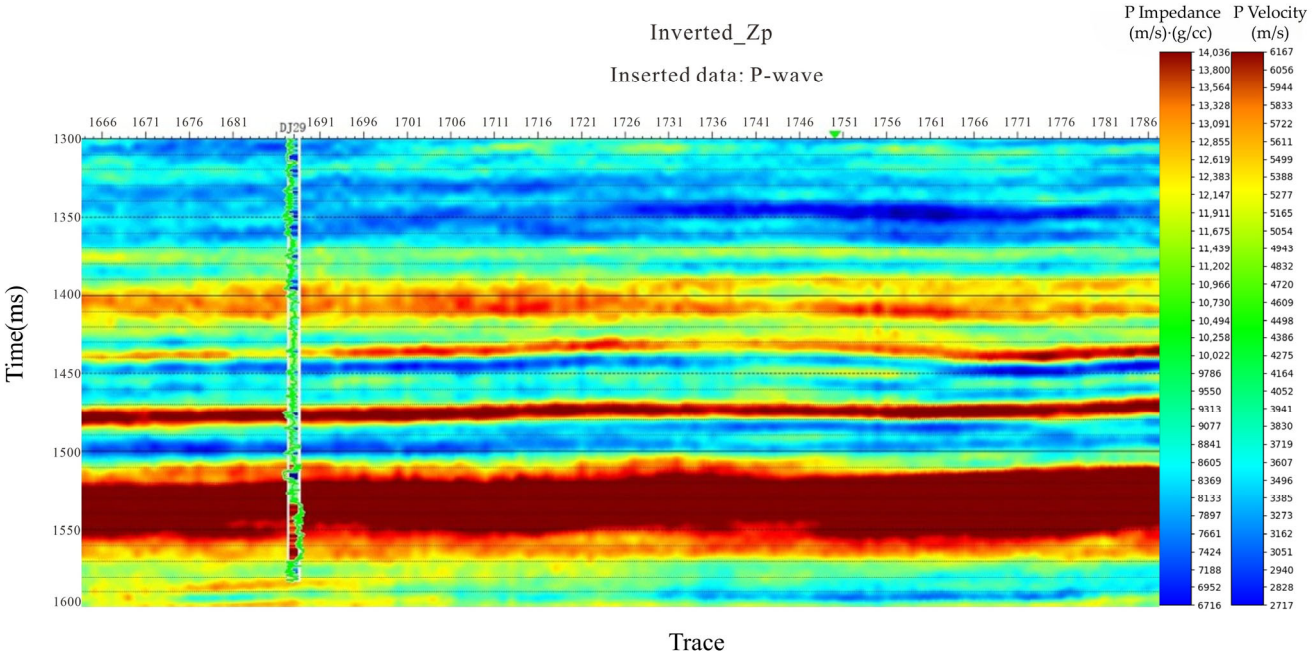


Figure 12. P-impedance section derived from the attenuation-compensated seismic data.

The P-impedance section reveals a clear, geologically plausible layering. The values, ranging from approximately 6716 to 14,036 ((m/s)·(g/cc)), are entirely consistent with the known lithologies in the area. While the overall structure exhibits lateral continuity, the section is simultaneously rich with the vertical detail necessary to characterize the complex stratigraphy of the Shanxi Formation.

Our primary target, the Shan-2 member, is clearly delineated. This unit, recognized as a deltaic sequence of interbedded mudstones, sandstones, and coal seams, is characterized by significant impedance contrasts [77,78]. The inversion successfully resolves this internal heterogeneity. Notably, a prominent, laterally continuous high-impedance layer (deep red hues, Z_p > 13,000 ((m/s)·(g/cc)) is imaged near 1500 ms, which strongly correlates with known coal-bearing strata within the Shan-2 member. Geologically, this high-impedance signature is characteristic of the dense, low-porosity coal seams that formed in the oxygen-poor swamp environments of the upper delta plain. The ability to clearly delineate these coal seams is critical, as they not only act as seismic masking layers but also serve as important stratigraphic markers separating different deltaic lobes and influencing vertical

reservoir connectivity. Immediately above this high-impedance zone, the section from 1400 ms to 1500 ms displays a more moderate impedance (yellow-orange hues), which corresponds to the organic-rich and sandy mudstones of the upper Shan-2 sub-members [79]. The overlaid P-wave log at the DJ29 well location exhibits an excellent match with the inverted impedance, thereby lending high confidence to these lithological interpretations. Ultimately, this detailed and well-calibrated impedance volume transcends the definition of a merely improved image; it represents a quantitative representation of the subsurface, enabling a highly reliable prediction of the reservoir's key properties.

To quantitatively evaluate the benefits of the attenuation compensation workflow, we first established a reference dataset for comparison. An identical post-stack simultaneous inversion was performed using the original, uncompensated seismic data, thereby creating a benchmark representing the best possible outcome from a conventional approach. The resulting P-impedance volume is presented in Figure 13's cross-section.

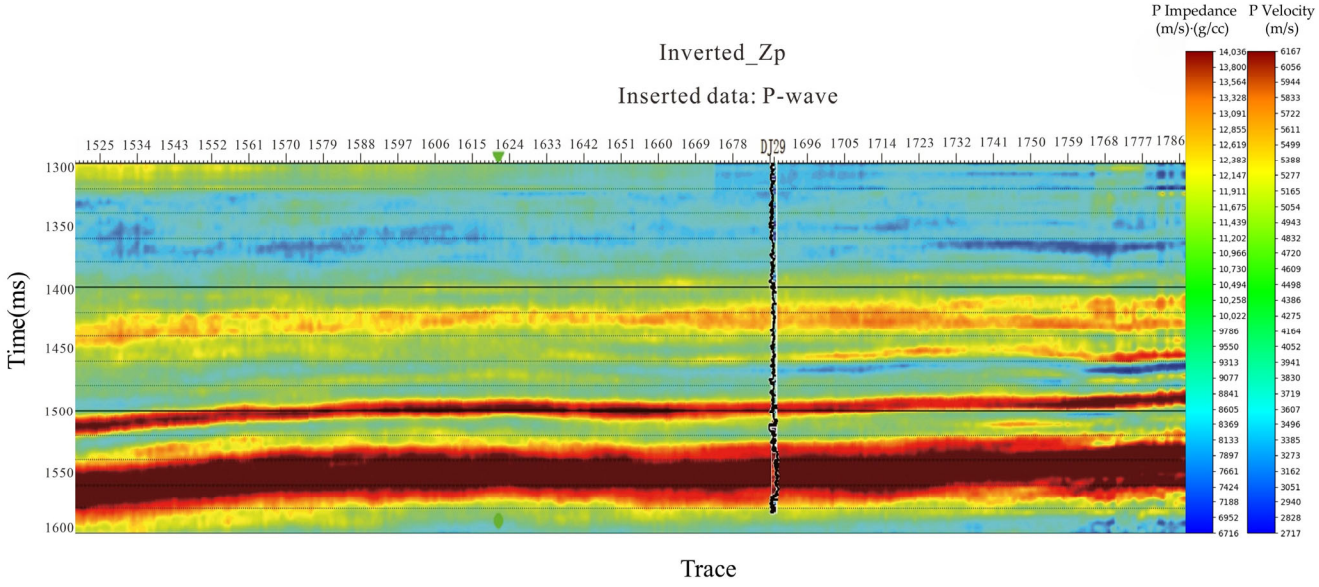


Figure 13. P-impedance section derived from well-constrained seismic inversion.

At a cursory glance, this conventional result appears geologically plausible: it captures the main structural elements and the large-scale impedance contrasts, exhibiting a reasonable overall match with the overlaid DJ29 well log. However, a more critical analysis immediately reveals the profound deficiencies imposed by the lower-bandwidth, phase-distorted input data—limitations that directly impede reliable reservoir characterization.

Within the target Shan-2 member, the stratigraphic details essential for understanding the reservoir architecture remain blurred. The boundaries between sandstones, shales, and thin coal seams are diffuse, with their distinct impedance signatures smeared into an averaged, ambiguous response. This loss of resolution constitutes not a minor flaw, but a critical failure that prevents the delineation of individual flow units and baffles. This result perfectly exemplifies a fundamental challenge in quantitative interpretation: the most sophisticated inversion algorithm cannot recover geological detail irrevocably lost due to seismic attenuation. Consequently, the fidelity of the final model is irrevocably capped by the quality of the input seismic data.

This conventional result, therefore, serves as more than a simple benchmark. It starkly defines the specific problem our framework is designed to solve, setting the stage for demonstrating a substantial improvement in capability: transitioning from a blurry, generalized image of the subsurface to a high-fidelity model capable of underpinning reliable predictions of critical reservoir parameters like TOC and porosity.

The inability of the conventional approach to achieve the required stratigraphic detail underscores the necessity of maximizing input data fidelity, a requirement addressed directly by our attenuation compensation workflow. The effectiveness of the Q-compensated seismic data is pivotal for resolving the complex heterogeneity of the Shan-2 member. Seismic attenuation, primarily caused by the thick overburden and multiple coal seams, severely attenuates high frequencies and introduces phase distortion. This physical mechanism directly compromises the vertical resolution, causing distinct impedance interfaces (e.g., coal-sand boundaries) to smear into ambiguous, low-fidelity responses.

By applying inverse Q-filtering prior to inversion, two critical geophysical improvements are realized, directly influencing the characterization of the Shan-2 member's heterogeneity:

Vertical Resolution Enhancement: The effective bandwidth of the seismic wavelet is restored to higher frequencies, which dramatically reduces the tuning thickness of the wavelet, enabling the inversion to successfully delineate the thin interbedded layers characteristic of the Shan-2 deltaic sequence.

Impedance Contrast Fidelity: Phase distortion is corrected, and the amplitude loss is compensated for, ensuring that the inverted acoustic impedance values accurately reflect the true magnitude of the impedance contrasts between different lithologies (sandstone, mudstone, and coal).

The preservation of high-frequency detail and amplitude integrity is a critical step: it transforms the P-impedance volume into a high-fidelity quantitative attribute, thereby establishing the reliable foundation required for an effective Total Organic Carbon (TOC) and porosity characterization.

4.3.3. Unlocking Higher-Fidelity Reservoir Parameter Prediction

The superior resolution of the P-impedance volume, derived from the attenuation-compensated framework, constitutes a robust foundation for quantitative reservoir characterization. This crucial step effectively bridges the gap between a refined geophysical attribute and actionable geological insight. By applying a multi-regression petrophysical model established from well data (Equation (15)), the high-fidelity P-impedance data is transformed into a Total Organic Carbon (TOC) volume, enabling a detailed investigation of the hydrocarbon source rock potential.

$$y = 0.0006x - 1.4236 \quad (15)$$

In the equation, x represents the Total Organic Carbon (TOC) in weight percent (wt%), and y represents the longitudinal wave impedance in (m/s)·(g/cc). This equation reveals the relationship between these two parameters, allowing for the calculation of TOC data volumes across the entire study area.

Figure 14a presents the resulting TOC prediction profile, passing directly through the calibration well DJ29. The improvement realized over conventional methods is immediately apparent. Where a standard inversion typically yields blurry, over-smoothed estimates, our result delineates the organic-rich intervals with exceptional clarity and geological realism. The profile reveals a thick, laterally continuous source rock interval, distinguished by vibrant red and dark-red hues corresponding to TOC values peaking at approximately 7%. Crucially, this zone is not a homogenous block; rather, it displays subtle internal variations in organic richness—details that were previously lost in the noise or filtered out by conventional processing. The predicted TOC values show excellent correlation with the inserted log data from well DJ29, thereby validating the accuracy of our model and the underlying impedance data. The sharp, well-defined boundaries at the top and bottom of this high-TOC layer underscore the enhanced vertical resolution, enabling a more precise estimation of the source rock's net thickness.

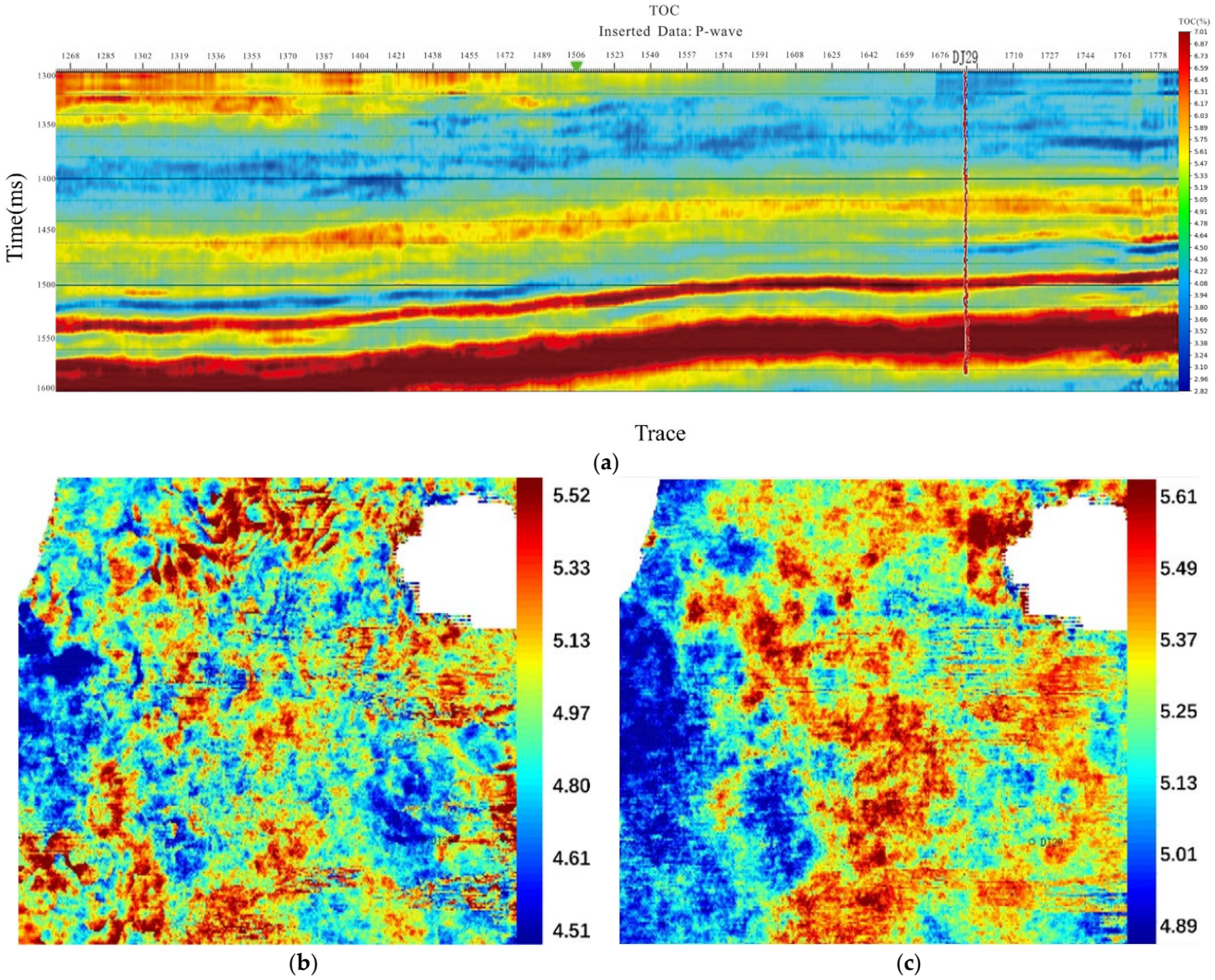


Figure 14. Predicted TOC distribution in the target interval. (**a**) A vertical TOC profile where the horizontal axis represents the Trace Number and the vertical axis is the two-way travel time (ms). (**b**,**c**) The TOC prediction maps of the top and bottom of the Shanxi Formation Shan-23 submember.

While the vertical profile confirms the presence and richness of the source rock, its lateral distribution is paramount for understanding the depositional system and identifying the most prolific "hydrocarbon kitchens." Accordingly, we extracted TOC attribute maps along the key stratigraphic horizons of the Shan-23 member. Figure 14b displays the TOC distribution along the top surface, and Figure 14c maps the TOC along its base.

A comparative analysis of these two maps yields critical geological insights. Spatially, both surfaces confirm a consistent trend: the primary centers of organic matter accumulation are concentrated in the eastern and southeastern portions of the study area. This spatial pattern is interpreted to reflect the paleo-depositional setting of the Shan-2 member. These areas likely correspond to the more distal, lower-energy parts of the deltaic system or protected interdistributary bays. In these settings, reduced clastic input and anoxic bottom-water conditions would have promoted the widespread preservation of organic matter, leading to the formation of thick, high-quality source rocks. These regions thus emerge as the depositional sweet spots, representing the most favorable zones for hydrocarbon generation. However, a significant vertical difference in organic richness is observed between the two surfaces. Specifically, the basal layer of Shan-23 (Figure 14c) exhibits a generally higher and more widespread organic enrichment, with TOC values ranging from a minimum of approximately 4.89% to a peak of 5.61%. This vertical trend

suggests a transgressive-regressive cycle, where the initial flooding event at the base of Shan-23 created the most widespread anoxic conditions ideal for source rock deposition. Subsequent progradation of the delta may have led to slightly more oxygenated conditions, resulting in the comparatively lower TOC at the top surface. This range is consistently higher than the values observed on the top surface. This distinct vertical gradient suggests a depositional history where the most anoxic and favorable conditions for organic matter preservation occurred during the initial stages of the Shan-23 member's formation. As deposition continued, conditions may have become slightly less favorable, resulting in the comparatively lower TOC at the top surface.

This detailed, three-dimensional characterization of TOC—delineating not only the high-potential geographic areas but also the most enriched intervals within the vertical succession—constitutes a substantial enhancement of predictive capability. It moves beyond simple anomaly-finding to provide a geologically sound model of the source rock system that supports the refinement of future exploration strategies and the identification of highly prospective drilling targets.

While Total Organic Carbon (TOC) analysis successfully delineates the hydrocarbon source kitchens, the economic viability of the reservoir fundamentally hinges on its capacity to store and transmit these hydrocarbons. Specifically, porosity is the key parameter governing this storage capacity. Building upon the same high-fidelity, attenuation-compensated P-impedance volume, a corresponding multi-regression model (Equation (16)) was employed to derive a quantitative porosity volume for the entire study area.

$$y = 7 \times 10^{-5}x - 0.227 \quad (16)$$

This equation establishes the empirical relationship between porosity (x) in percent (%) and P-wave impedance (y) in (m/s)·(g/cc). It serves as the petrophysical transform to convert the entire impedance volume into a corresponding porosity volume for the study area.

The resulting porosity volume, visualized in the cross-well profile of Figure 15a, provides a significantly clearer picture of the reservoir's storage architecture. While confirming the overall low-porosity nature of the shale, a characteristic feature of such tight formations, our result moves beyond this general observation. The enhanced resolution, a direct benefit of the Q-compensated inversion, successfully resolves subtle, higher-porosity streaks and lenses that are typically smeared and averaged out in conventional inversion outputs. These discrete zones, indicated by the warmer colors, represent the most prospective storage intervals. The strong correlation with the DJ29 well log provides high confidence in the prediction, affirming that our methodology accurately captures even these minor variations in reservoir quality. The profile also reveals a distinct trend of decreasing porosity with depth, likely attributable to increased compaction and diagenetic effects, a phenomenon now imaged with high resolution and detail.

To elucidate the lateral heterogeneity of storage potential, we extracted porosity maps along the same Shan-23 horizons utilized for the TOC analysis. The map of the top surface (Figure 15b) reveals a well-defined, high-porosity fairway concentrated in the southwestern portion of the study area, which stands out as the primary sweet spot for hydrocarbon storage. From a sedimentological perspective, this southwestern high-porosity trend likely represents a more proximal, higher-energy part of the deltaic system, possibly corresponding to well-sorted distributary mouth bars or fluvial-dominated channel sands. In these environments, better sorting and lower mud content would have led to the preservation of higher primary porosity, creating effective reservoir facies. In contrast, the bottom surface (Figure 15c) exhibits a more uniformly distributed but generally lower porosity, thereby reinforcing the vertical compaction trend observed in the cross-well profile.

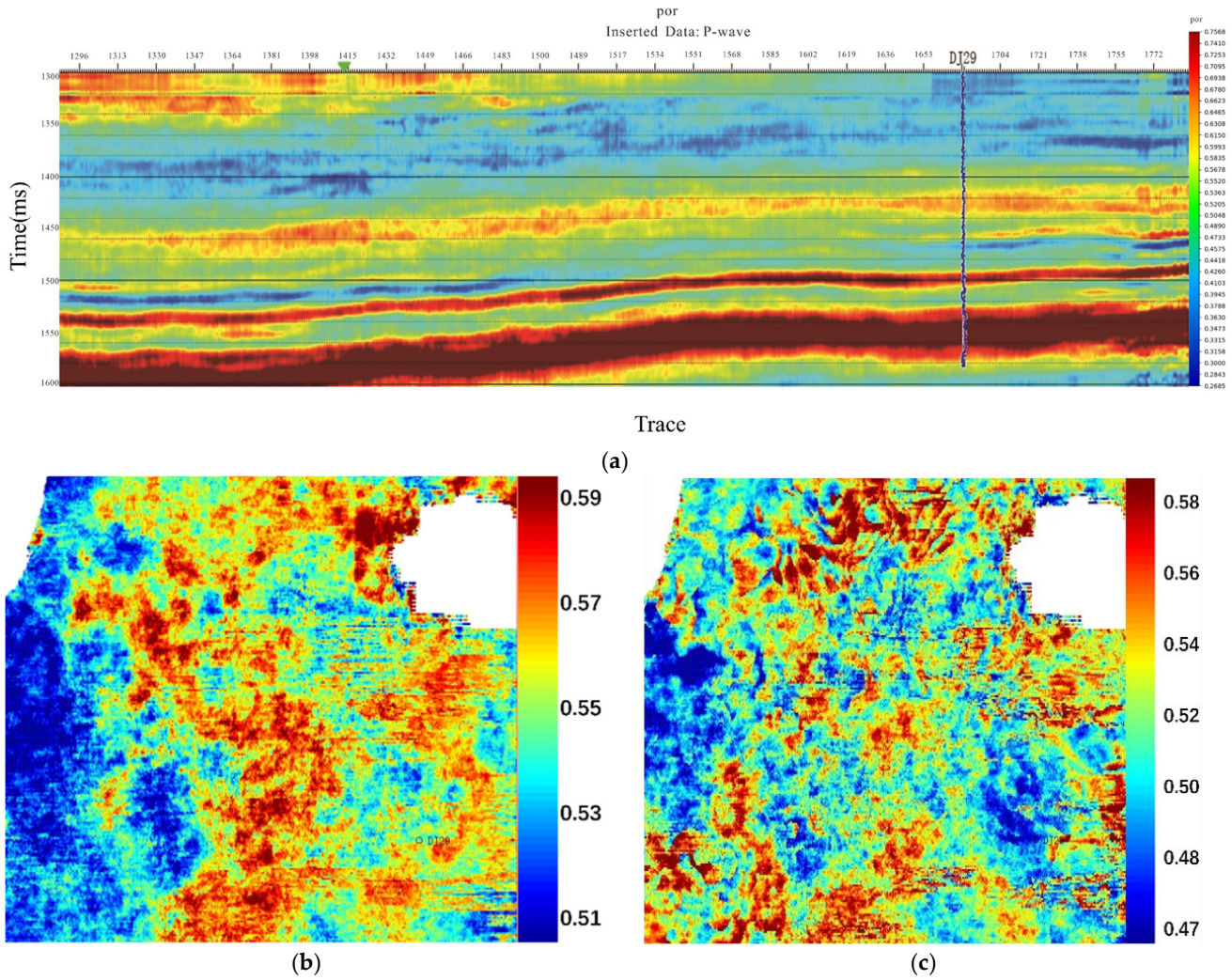


Figure 15. Predicted porosity distribution in the target interval: (**a**) cross-well porosity profile, (**b**) porosity map of the top horizon, and (**c**) porosity map of the bottom horizon. (**a**) Porosity profile with Trace Number on the x-axis and time (ms) on the y-axis. (**b**,**c**) The Porosity prediction map of the top and bottom of the Shanxi Formation Shan-23 submember.

A crucial integrated insight emerges from combining this porosity distribution with the previously discussed TOC map. This spatial partitioning between generation and storage zones is a critical finding, providing compelling geophysical evidence for a regional hydrocarbon migration model. It strongly suggests a primary migration pathway from the mature source kitchens in the east and southeast towards the higher-quality reservoir sweet spots in the southwest. Understanding this source-to-sink relationship is paramount for exploration, as it allows for the targeting of structures that lie along this inferred migration route, thereby increasing the probability of discovering charged reservoirs. The primary storage sweet spots in the southwest are geographically distinct from the main source kitchens identified in the east and southeast. This spatial partitioning between generation and storage zones is a critical finding, strongly suggesting a potential hydrocarbon migration pathway from east/southeast to southwest. Such detailed characterization proves invaluable for the development strategy. It permits the high-grading of drilling locations based not merely on a single attribute, but on the integrated understanding of both source richness and storage quality. This level of detail, which enables the clear distinction between source and reservoir domains, is a direct outcome of the superior imaging provided

by the advanced workflow. Ultimately, this transforms the geophysical dataset into an actionable tool for optimizing well placement and predicting production performance.

The distinct spatial partitioning revealed by this integrated analysis—between the primary source kitchens (east and southeast) and the optimal storage fairways (southwest)—provides a comprehensive and previously unresolvable picture of the reservoir's petroleum system. This clear geographic separation strongly suggests a potential hydrocarbon migration pathway, which constitutes a critical insight for understanding reservoir charge and accumulation mechanisms. This level of detailed characterization of reservoir heterogeneity, which clearly distinguishes source from storage, is a direct outcome of the enhanced resolution and fidelity provided by the Q-compensated impedance volume. This work transforms the reservoir from a generalized low-porosity, low-permeability challenge into a mappable system of distinct geological opportunities. This provides a robust framework for de-risking exploration and concentrating development efforts with enhanced confidence.

5. Conclusions

The core finding of this investigation demonstrates that in geologically complex, thin-bedded, and highly attenuating environments—such as those encountered in the Da Ning–Ji Xian area—the integration of physics-based Q-compensation is not an optional refinement but a critical prerequisite for achieving reliable quantitative seismic inversion. This work validates a critical paradigm shift: conventional amplitude-based workflows, despite their mathematical sophistication, are fundamentally constrained by the integrity of their input signal. By meticulously restoring the intrinsic amplitude and phase fidelity prior to inversion, this study ensures that the final impedance volumes are not merely plausible representations but possess the true diagnostic value required for accurate reservoir characterization.

The established attenuation-compensated inversion framework, anchored by the robust, high-resolution LTFT Q-estimation, yields three distinct and powerful contributions. Methodologically, it provides a verifiable, technically sound workflow that successfully resolves the complex, sub-seismic heterogeneity of the Shan-2 member, a challenge previously deemed intractable by conventional methods focused solely on post-inversion filtering. Importantly, although this study focuses on the Da Ning–Ji Xian area, the attenuation-compensated inversion framework is inherently generalizable. With appropriate adjustments to account for local geological heterogeneity and attenuation characteristics, the integrated LCFS–inverse Q–post-stack inversion workflow can be applied to other regions and even at a global scale. This establishes a reproducible methodology for tackling highly dissipative and structurally complex reservoirs beyond the studied area. Geophysically, the derived Q-field itself emerges as a critical diagnostic attribute, where low-Q anomalies conform precisely to organic-rich lithologies, offering an independent verification of reservoir complexity that surpasses traditional amplitude analysis. Geologically, the resulting high-fidelity TOC and porosity models unveil a clear and well-defined spatial partitioning between the source rock "kitchens" (hydrocarbon generation engine) and the primary reservoir "sweet spots" (storage fairways). This finding is paramount, as it delineates a dominant, regional-scale hydrocarbon migration pathway, fundamentally improving the exploration framework for de-risking charge and accumulation models.

Despite the robust results, it is important to acknowledge the inherent limitations of this study, which provide context for the interpretation. Firstly, the stability of the Q-field estimation is contingent on the local signal-to-noise ratio; in areas of poor data quality, the Q-model may carry higher uncertainty. Secondly, the post-stack inversion, like all inversion methods, is subject to non-uniqueness, with the final result being influenced

by the low-frequency model constructed from sparse well control. Perhaps most significantly, the prediction of TOC and porosity relies on empirical petrophysical transforms (Equations (15) and (16)) that assume a spatially constant relationship. This assumption may not fully capture lateral variations in mineralogy or diagenesis, meaning the derived property maps should be viewed as powerful indicators of trends and sweet spots rather than absolute point-by-point quantitative values.

These limitations, however, illuminate clear trajectories for future research. To enhance the Q-model's stability, future work should aim to integrate multi-scale constraints from Vertical Seismic Profile (VSP) or borehole seismic data. The challenge of non-uniqueness could be further addressed by advancing to pre-stack simultaneous inversion, which would incorporate valuable AVO information. Furthermore, transitioning from deterministic transforms to advanced geostatistical co-simulation is essential to quantify the uncertainty associated with the reservoir property predictions, thereby transforming single deterministic outcomes into a suite of risk-based models. Ultimately, the successful validation of this attenuation-compensated framework—bridging advanced seismic processing with profound geological insight—provides a transferable, industry-ready template for unlocking similar unconventional resources globally in complex, highly dissipative geological settings.

Author Contributions: Conceptualization, J.Z.; methodology, Y.Y.; software, Y.Y. and H.P.; validation, T.S.; investigation, Y.Y.; resources, Z.Q. and Q.Z.; data curation, Z.Q. and Q.Z.; writing—original draft preparation, Y.Y.; writing—review and editing, J.Z.; visualization, J.Z.; supervision, J.Z.; project administration, J.Z.; funding acquisition, J.Z. All authors have read and agreed to the published version of the manuscript.

Funding: This work is supported by the Science Fund for Creative Research Groups of the National Natural Science Foundation of China (No. 42321002) and Fundamental Research Funds for the Central Universities (Grant Nos. 2022JCCXMT01, 2602020RC130).

Institutional Review Board Statement: Not applicable.

Informed Consent Statement: Not applicable.

Data Availability Statement: The original contributions presented in this study are included in the article. Further inquiries can be directed to the corresponding author.

Acknowledgments: We would like to express our gratitude to the Editor-in-Chief and the two anonymous reviewing experts for their valuable comments and feedback on this manuscript.

Conflicts of Interest: Authors Qin Zhang and Zhen Qiu were employed by the companies PetroChina Research Institute of Petroleum Exploration and Development and National Energy Shale Gas R & D (Experiment) Center. The remaining authors declare that the research was conducted in the absence of any commercial or financial relationships that could be construed as a potential conflict of interest.

References

1. Li, Y.; Duan, W.; Qin, L.; Zheng, D.; Wang, X.; Liu, L. Adjacent channel attenuation difference estimation and its application in near-surface Q inversion. *J. Appl. Geophys.* **2023**, *215*, 105064. [CrossRef]
2. Liu, W.; Li, Z.; Huang, X.; Qin, H.; Xie, Y.; Chen, K.; Zhang, Z. Seismic Attenuation Parameter Estimation Based on Improved GLCT. *IEEE Geosci. Remote Sens. Lett.* **2024**, *21*, 3004605. [CrossRef]
3. Zhang, Q.; Lv, X.-y.; Lei, Q.; Peng, B.; Li, Y.; Zhang, Y.-w. Seismic multiple attenuation based on improved U-Net. *Appl. Geophys.* **2024**, *21*, 680–696. [CrossRef]
4. Liu, W.; Zhai, Z.; Fang, Z. A multisynchrosqueezing-based S-transform for time-frequency analysis of seismic data. *Pure Appl. Geophys.* **2025**, *182*, 1279–1295. [CrossRef]
5. Yin, Z.; Wei, J.; Di, B. Identification of fracture strike using Q-anisotropy. *Pet. Geophys. Prospect.* **2011**, *46*, 429–433. [CrossRef]
6. Bose, S.; Singh, C.; Sarkar, S.; Dutta, A. Crustal Heterogeneity of the Bhutan Himalaya: Insights from PgQ Tomography. *Bull. Seismol. Soc. Am.* **2025**, *115*, 248–259. [CrossRef]

7. Duan, M.; Zhou, L.; Fu, Y.; An, Y.; Yang, J.; Zhang, X. The 3D QP model of the China Seismic Experimental Site (CSES-Q1.0) and its tectonic implications. *Solid Earth* **2025**, *16*, 391–408. [CrossRef]
8. Peng, Z.; Qu, J.; Chen, C.; Wang, H.; Zhu, D.; Mi, Z.; Xie, E.; Zhang, Z.; Yu, X.; Wang, H. Coal Accumulation in Marine to Continental Transitional Sequence During Late Carboniferous-Early Permian in the Southeastern Ordos Basin, China. *Geol. J.* 2025; *early access*. [CrossRef]
9. Qi, Y.; Wu, K.; Li, Q.; Zheng, X.; Wang, B.; Li, D.; Tang, W. Seismic prediction technology for thin reservoirs of tight gas in coal measure strata: A case study of Block L in the eastern margin of the Ordos Basin. *Front. Earth Sci.* **2025**, *12*, 1487487. [CrossRef]
10. Zhang, K.; Li, S.; Zhong, G.; Feng, P.; Chang, C.; Li, H. Characteristics of in-situ stress field of coalbed methane reservoir in the eastern margin of Ordos basin. *Int. J. Coal Geol.* **2025**, *301*, 104715. [CrossRef]
11. Seelam, N.K.; Kumar, T.; Dhubia, S.; Rao, G.S.; Pal, S.K. Enhancing Thin Coal Seam Detection in Eastern Indian Coalfields Using ICWT-Decon-Based Seismic Attributes and Acoustic Impedance Inversion. *Minerals* **2024**, *14*, 920. [CrossRef]
12. Wang, X.; Zhou, L.; Wu, Y.; Li, S.; Gu, Y.; Li, X. Factors controlling spatial distribution of complex lithology in transitional shale strata: Implications from logging and 3D seismic data, Shan-2 Lower Sub-member, Eastern Ordos Basin. *Front. Earth Sci.* **2023**, *10*, 951524. [CrossRef]
13. Yu, H.; Wang, H.; Wu, L.; Chen, T. A precise time-depth conversion method for coal seam based on machine learning and seismic velocity inversion. *Acta Geophys.* **2025**, *73*, 4059–4073. [CrossRef]
14. Wu, H.; Zhu, S.; Liu, Q.; Dong, S.; Huang, Y.; Zhang, P. Amplitude variation with offset and azimuth inversion to predict and evaluate coal seam fracture parameters. *Front. Earth Sci.* **2023**, *17*, 505–513. [CrossRef]
15. Veeken, P.; Da Silva, M. Seismic inversion methods and some of their constraints. *First Break* **2004**, *22*, 2004. [CrossRef]
16. Gholami, A. A fast automatic multichannel blind seismic inversion for high-resolution impedance recovery. *Geophysics* **2016**, *81*, V357–V364. [CrossRef]
17. Zhang, B.; Pu, Y.; Dai, R.; Cao, D. Seismic poststack impedance inversion using geophysics-informed deep-learning neural network. *Interpretation* **2025**, *13*, T219–T232. [CrossRef]
18. Zhao, Y.; Wen, X.; Xie, C.; Li, B.; Pan, X.; Zhou, X.; Li, C. Seismic inversion of anisotropic and isotropic fluid indicators and fracture density in the TTI medium. *IEEE Trans. Geosci. Remote Sens.* **2025**, *63*, 5911821. [CrossRef]
19. Arabpour, A.; Hamidzadeh Moghadam, R.; Niri, M.E. Bayesian seismic inversion by residual flow. *Geophysics* **2025**, *90*, R345–R362. [CrossRef]
20. Jing, S.; Dengfa, H. Tectonic characteristics and evolution of the middle segment of the Jinxi flexure fold belt in the eastern margin of the Ordos Basin. *Chin. J. Geol.* **2024**, *59*, 723–731. [CrossRef]
21. Liu, S. The coupling mechanism of basin and orogen in the western Ordos Basin and adjacent regions of China. *J. Asian Earth Sci.* **1998**, *16*, 369–383. [CrossRef]
22. Dengfa, H.; Cheng, X.; Zhang, G.; Wenzhi, Z.; Zhe, Z.; Xinshe, L.; Hongping, B.; Liyong, F.; Song, Z.; Baize, K. Scope, nature, and exploration significance of Ordos Basin during geological historical periods, NW China. *Pet. Explor. Dev.* **2025**, *52*, 855–871. [CrossRef]
23. Liu, J.; Liu, K.; Huang, X. Effect of sedimentary heterogeneities on hydrocarbon accumulations in the Permian Shanxi Formation, Ordos Basin, China: Insight from an integrated stratigraphic forward and petroleum system modelling. *Mar. Pet. Geol.* **2016**, *76*, 412–431. [CrossRef]
24. Liu, S.; Li, J.; Jin, F.; Liu, H.; Wang, M.; Cheng, Y.; Zhong, X.; Lu, H. Genesis of efficient reservoirs in mixed sedimentary setting: A case study of Benxi Formation in the Gaoqiao area, Ordos Basin. *Turk. J. Earth Sci.* **2024**, *33*, 118–145. [CrossRef]
25. Guo, W.; Shen, W.; Zhou, S.; Xue, H.; Liu, D.; Wang, N. Shale favorable area optimization in coal-bearing series: A case study from the Shanxi Formation in Northern Ordos Basin, China. *Energy Explor. Exploit.* **2018**, *36*, 1295–1309. [CrossRef]
26. Chen, Y.; Zhao, J.; Guo, M.; Wang, Y.; Wu, H.; Li, J.; Wu, W. Depositional process and its control on the densification of coal-measure tight sandstones: Insights from the Permian Shanxi Formation of the northeastern Ordos Basin, China. *Int. J. Earth Sci.* **2023**, *112*, 1871–1890. [CrossRef]
27. Zhao, W.-B.; Zhang, H.; Shi, Y.-H.; Fu, X.-X.; Hui, J.; Jing, X.-Y. Geological characteristics and exploration potential of the coal measure gas from Shan 2 of the Shanxi formation in the eastern Ordos Basin. *Front. Earth Sci.* **2023**, *11*, 1142141. [CrossRef]
28. Liu, Z.; Zhao, S.; Hu, Z.; Shen, B.; Feng, D.; Zhang, J.; Ye, J.; Ma, C.; Dong, Z. Characteristics and controlling factors of coal-measure unconventional reservoirs—A case study of the Carboniferous-Permian in the Ordos Basin. *Unconv. Resour.* **2025**, *6*, 100153. [CrossRef]
29. Tao, H.; Cui, J.; Zhao, F.; Ren, Z.; Qi, K.; Liu, H.; Su, S. Thermal history and hydrocarbon accumulation stages in Majiagou Formation of Ordovician in the East-Central Ordos Basin. *Energies* **2024**, *17*, 4435. [CrossRef]
30. Fang, X.; Qiu, F.; Shu, L.; Huo, Z.; Li, Z.; Cai, Y. Reservoir Properties and Gas Potential of the Carboniferous Deep Coal Seam in the Yulin Area of Ordos Basin, North China. *Energies* **2025**, *18*, 3987. [CrossRef]
31. Zhao, W.; Wen, Z.; Zhang, H.; Wu, C.; Liu, Y.; Song, H.; Zhang, L.; Xi, Y.; Sun, L. Integrated assessment of marine-continental transitional facies shale gas of the carboniferous Benxi Formation in the Eastern Ordos Basin. *Energies* **2021**, *14*, 8500. [CrossRef]

32. Chen, S.; Xu, Y.; Yu, Y.; Feng, J.; Yuan, S. Geologically Guided Sparse Multitrace Reflectivity Inversion for High-Resolution Characterization of Subtle Reservoirs. *Appl. Sci.* **2025**, *15*, 5125. [CrossRef]
33. Qi, Y.; Wu, K.; Wang, B.; Zheng, X.; Li, W.; Li, D. Lithofacies identification of deep coalbed methane reservoir based on high-resolution seismic inversion. *Front. Earth Sci.* **2024**, *12*, 1440729. [CrossRef]
34. Basin, T. Analysis of Seismic Response Characteristics of Coal-Bearing Sandstone Reservoirs in the Middle and Lower Jurassic in the South. In Proceedings of the International Field Exploration and Development Conference 2023: Volume 2, Wuhan, China, 19–21 September; Springer Nature: Berlin/Heidelberg, Germany, 2024; p. 234. [CrossRef]
35. Lihong, Z.; Yong, L.; Rong, D.; Wei, H.; Yongzhou, L.; Hui, M.; Haijiao, F.; Yi, D.; Zhitong, Z.; Zhuangsen, W. Differential accumulation characteristics and production of coalbed methane/coal-rock gas: A case study of the No. 8 coal seam of the Carboniferous Benxi Formation in the Daji block, Ordos Basin, NW China. *Pet. Explor. Dev.* **2025**, *52*, 872–882. [CrossRef]
36. Liyuan, L.; Yong, L.; Shuxin, L.; Qingbo, H.; Shijia, C.; Xiang, L.; Xingtao, L.; Jungang, L.; Zhenglu, X.; Xiangdong, Y. Controlling factors of Marine and continental transitional shale gas enrichment in Shan2 3 sub-member, Daji area, eastern margin of Ordos Basin. *Nat. Gas Geosci.* **2025**, *36*, 554–566. [CrossRef]
37. Lin, H.; Liu, X.; Xiong, J.; Liang, L.; Ding, Y.; Wu, J.; Li, B. Research on transversely isotropic in-situ stress logging prediction of transitional shale reservoir: A case study of Daji Block, Eastern Ordos Basin, North China. *Pet. Sci. Technol.* **2024**, *42*, 1296–1315. [CrossRef]
38. Yan, T.; He, S.; Zheng, S.; Bai, Y.; Chen, W.; Meng, Y.; Jin, S.; Yao, H.; Jia, X. Critical tectonic events and their geological controls on deep buried coalbed methane accumulation in Daning-Jixian Block, eastern Ordos Basin. *Front. Earth Sci.* **2023**, *17*, 197–217. [CrossRef]
39. Zhang, L.; Dong, D.; Qiu, Z.; Wu, C.; Zhang, Q.; Wang, Y.; Liu, D.; Deng, Z.; Zhou, S.; Pan, S. Sedimentology and geochemistry of Carboniferous-Permian marine-continental transitional shales in the eastern Ordos Basin, North China. *Palaeogeogr. Palaeoclimatol. Palaeoecol.* **2021**, *571*, 110389. [CrossRef]
40. Kuang, L.; Dazhong, D.; Wenyuan, H.; Shengming, W.; Shasha, S.; Shuxin, L.; Zhen, Q.; Xinwei, L.; Yong, L.; Jin, W. Geological characteristics and development potential of transitional shale gas in the east margin of the Ordos Basin, NW China. *Pet. Explor. Dev.* **2020**, *47*, 471–482. [CrossRef]
41. Pan, B.; Wang, K.; Dong, G.; Zhou, X.; Chen, Y.; Zhuang, Y.; Gao, X.; Du, X. Geochemical Characteristics and Paleoenvironmental Significance of No. 5 Coal in Shanxi Formation, Central–Eastern Ordos Basin (China). *Minerals* **2025**, *15*, 177. [CrossRef]
42. Qiu, Y.; Wang, H.; Guo, G.; Mo, R.; Pan, Z.; Cai, Y.; Abuduerxiti, A. Gas distribution and its geological factors in the No. 5 coal seam of the Weibei field, Southeastern Ordos Basin, North China. *Processes* **2022**, *10*, 659. [CrossRef]
43. Peng, H.J.; Zhao, J.T.; Qiu, Z.; Zhang, Q.; Liu, W.; Kong, W.L.; Gao, W.L.; Sheng, T.J.; Li, W.Y.; Yang, Y.G. Multi-scale fracture characterization method for transitional shale reservoir based on post-stack multi-attribute ant-tracking fusion and pre-stack wide-azimuth gathers AVAZ analysis. *Geomech. Geophys. Geo-Energy Geo-Resour.* **2025**, *11*, 13. [CrossRef]
44. Wang, D.-X.; Wang, Y.-G.; Zhao, Y.-H.; Tian, R.-F.; Xue, Y.-J. A strong seismic reflection amplitude suppressing method applied in the Ordos Basin. In Proceedings of the SPG/SEG 2016 International Geophysical Conference, Beijing, China, 20–22 April 2016; pp. 389–391. [CrossRef]
45. Rongtao, G.; Yun, C.; Ziqi, T.; Zhao, L. Data Processing Solutions on Low Signal-to-Noise Data in Loess Plateau Area-A Case Study in Ordos Basin, China. *CT Theory Appl.* **2025**. [CrossRef]
46. Zhang, J.; Gao, N.; Huang, L.-G.; Li, Q.-Y.; Ge, B.-Y. Seismic Prediction of Laminated-Type Shale Oil Reservoirs and Its Application in Qingcheng Area, Ordos Basin. In Proceedings of the International Field Exploration and Development Conference, Xi'an, China, 12–14 September 2024; Springer: Berlin/Heidelberg, Germany; pp. 917–927. [CrossRef]
47. Manzoor, U.; Ehsan, M.; Hussain, M.; Bashir, Y. Improved reservoir characterization of thin beds by advanced deep learning approach. *Appl. Comput. Geosci.* **2024**, *23*, 100188. [CrossRef]
48. Chen, Z.; Li, X.; Chen, H.; Duan, Z.; Qiu, Z.; Zhou, X.; Hou, Y. The characteristics of lithofacies and depositional model of fine-grained sedimentary rocks in the Ordos Basin, China. *Energies* **2023**, *16*, 2390. [CrossRef]
49. Zhou, C.; Liu, Z.; Zhang, L.; Dai, D.; Zhang, L.; Li, C.; Shi, Y.; Liu, G. Applications of NMR logs to complex lithology interpretation of ordos basin. In Proceedings of the SPWLA Annual Logging Symposium, Austin, TX, USA, 3–6 June 2007; p. SPWLA–2007-JJJ.
50. Huang, Z.; Zhou, R.; Yang, J.; Wang, M.; Wang, D.; Ma, Z.; Qi, L.; Men, X.; Fang, L. Study on optimization of well pattern and well spacing for CBM development: Taking Daning Block as an example. *Coal Sci. Technol.* **2023**, *51*, 121–131. [CrossRef]
51. Wanghua, S. Catastrophic mechanism of seepage deformation and failure of mining rock mass and its prevention & control I: Water-sand mixture inrush from seam roof. *J. Earth Sci. Environ.* **2022**, *44*, 903–921. [CrossRef]
52. Quan, Y.; Harris, J.M. Seismic attenuation tomography using the frequency shift method. *Geophysics* **1997**, *62*, 895–905. [CrossRef]
53. Fomel, S. Shaping regularization in geophysical-estimation problems. *Geophysics* **2007**, *72*, R29–R36. [CrossRef]
54. Fomel, S. Local seismic attributes. *Geophysics* **2007**, *72*, A29–A33. [CrossRef]
55. Wang, Y. Inverse Q-filter for seismic resolution enhancement. *Geophysics* **2006**, *71*, V51–V60. [CrossRef]

56. Alshangiti, A.; Zhou, H.W. Estimation of seismic attenuation for reservoirs mapping and inverse Q-filtering: An application on land seismic data. *Geophys. Prospect.* **2023**, *71*, 682–697. [CrossRef]
57. Wang, Y. *Seismic Inverse Q Filtering*; John Wiley & Sons: Hoboken, NJ, USA, 2009.
58. Maurya, S.; Singh, N.; Singh, K. Post-stack seismic inversion. In *Seismic Inversion Methods: A Practical Approach*; Springer: Berlin/Heidelberg, Germany, 2020; pp. 39–80. [CrossRef]
59. Kumar, R.; Das, B.; Chatterjee, R.; Sain, K. A methodology of porosity estimation from inversion of post-stack seismic data. *J. Nat. Gas Sci. Eng.* **2016**, *28*, 356–364. [CrossRef]
60. Sotelo, V.; Almanza, O.; Montes, L. Post-stack seismic inversion through probabilistic neural networks and deep forward neural networks. *Earth Sci. Inform.* **2024**, *17*, 1957–1966. [CrossRef]
61. Shakir, U.; Ali, A.; Hussain, M.; Azeem, T.; Bashir, L. Selection of sensitive post-stack and pre-stack seismic inversion attributes for improved characterization of thin gas-bearing sands. *Pure Appl. Geophys.* **2022**, *179*, 169–196. [CrossRef]
62. Pramudito, D.; Harisandi, A.; Sinaga, R.P.; Nuraeni, F. Enhancing Low-Frequency Model for Post-Stack Inversion using Geostatistics: A Case Study in Imaging Carbonate Structure. *J. Geofis.* **2021**, *19*, 69–73. [CrossRef]
63. Datta Gupta, S.; Sinha, S.K.; Chahal, R. Capture the variation of acoustic impedance property in the Jaisalmer Formation due to structural deformation based on post-stack seismic inversion study: A case study from Jaisalmer sub-basin, India. *J. Pet. Explor. Prod. Technol.* **2022**, *12*, 1919–1943. [CrossRef]
64. Das, B.; Chatterjee, R. Porosity mapping from inversion of post-stack seismic data. *Georesursy* **2016**, *18*, 306–313. [CrossRef]
65. El-Sayed, A.S.; Mabrouk, W.M.; Metwally, A.M. Utilizing post-stack seismic inversion for delineation of gas-bearing sand in a pleistocene reservoir, baltim gas field, nile delta, Egypt. *Sci. Rep.* **2024**, *14*, 29596. [CrossRef]
66. Xue, Y.-J.; Cao, J.-X.; Wang, X.-J.; Du, H.-K. Estimation of seismic quality factor in the time-frequency domain using variational mode decomposition. *Geophysics* **2020**, *85*, V329–V343. [CrossRef]
67. Bouchaala, F.; Ali, M.Y.; Matsushima, J.; Bouzidi, Y.; Jouini, M.S.; Takougang, E.M.; Mohamed, A.A. Estimation of seismic wave attenuation from 3D seismic data: A case study of OBC data acquired in an offshore oilfield. *Energies* **2022**, *15*, 534. [CrossRef]
68. Liu, Y.; Fomel, S. Seismic data analysis using local time-frequency decomposition. *Geophys. Prospect.* **2013**, *61*, 516–525. [CrossRef]
69. Sun, H.; Xu, R.; Zhang, J.; Huang, X.; Han, L. A Modified Unscaled S-Transform for Seismic Time-Frequency Analysis of Road Detection in Intelligent Transportation Systems. *IEEE Trans. Intell. Transp. Syst.* 2025, *early access*. [CrossRef]
70. Ma, S.; Cao, J. An Efficient Transformer Model Enhanced by S-transform and Transfer Learning for Predicting Gas Distribution in Deeply Buried Reservoirs. *IEEE Trans. Geosci. Remote Sens.* **2025**, *63*, 5910414. [CrossRef]
71. Ba, J.; Ba, X.-Y.; Dong, H.-J.; Cheng, J.-W.; Luo, C.; Yang, Z.-F.; Pang, M.-Q.; Tan, W.-H. Reservoir property estimation of interbedded sandstone and shale layers using segmented 3D rock-physics templates. *Appl. Geophys.* **2025**, 1–17. [CrossRef]
72. Fawei, M.; Yanxiao, H.; Zhengxin, T.; Shengbo, Y.; Jingyang, N. A seismic reservoir characterization method based on post and pre-stack joint inversion. *Pet. Sci. Bull.* **2025**, *10*, 666. [CrossRef]
73. Samuel, S.A. *Integrated Post-Stack Seismic Inversion, Multi-Attribute Analysis, and Machine Learning for Carbon Storage*; Oklahoma State University: Stillwater, OK, USA, 2025. Available online: https://hdl.handle.net/20.500.14446/346428 (accessed on 22 October 2025).
74. Liu, S.; Zhou, L.; Zhang, B.; Dai, R.; Lu, P.; He, C.; Wu, Y.; Ni, C. Thin-Layer Siliceous Dolomite Prediction Based on Post-Stack Seismic Data Mining and Optimization. *Appl. Sci.* **2025**, *15*, 9631. [CrossRef]
75. Li, M.; Huang, X.; Tang, S.; Chen, K.; Ran, Q. Reservoir-oriented migrated seismic image improvement and poststack seismic inversion using well-seismic mistie. *Interpretation* **2025**, *13*, T99–T112. [CrossRef]
76. Kirkevik, T. Simultaneous Inversion of Post-Stack Seismic Time-Lapse Data. In Proceedings of the 86th EAGE Annual Conference & Exhibition, Toulouse, France, 2–5 June 2025; European Association of Geoscientists & Engineers: Bunnik, The Netherlands, 2025; pp. 1–5. [CrossRef]
77. Cai, G.; Gu, Y.; Song, D.; Jiang, Y.; Fu, Y.; Liu, Y.; Zhang, F.; Lu, J.; Qiu, Z. Gas occurrence characteristics in marine-continental transitional shale from Shan23 sub-member shale in the Ordos Basin: Implications for shale gas production. *Nat. Gas Ind. B* **2025**, *12*, 368–385. [CrossRef]
78. Chen, M.; Wang, B.; Tian, H.; Sun, J.; Liu, L.; Liang, X.; Chen, B.; Yu, B.; Zhang, Z. Multilayer Gas-Bearing System and Productivity Characteristics in Carboniferous–Permian Tight Sandstones: Taking the Daning–Jixian Block, Eastern Ordos Basin, as an Example. *Energies* **2025**, *18*, 2398. [CrossRef]
79. Zhang, J.; Dang, W.; Zhang, Q.; Wang, X.; Du, G.; Shan, C.; Lei, Y.; Shangguan, L.; Xue, Y.; Zhang, X. Fractal Characterization of Pore Structures in Marine–Continental Transitional Shale Gas Reservoirs: A Case Study of the Shanxi Formation in the Ordos Basin. *Energies* **2025**, *18*, 4013. [CrossRef]

Disclaimer/Publisher's Note: The statements, opinions and data contained in all publications are solely those of the individual author(s) and contributor(s) and not of MDPI and/or the editor(s). MDPI and/or the editor(s) disclaim responsibility for any injury to people or property resulting from any ideas, methods, instructions or products referred to in the content.